A fully-coupled analysis of the spar-type floating offshore wind turbine with bionic fractal heave plate under wind-wave excitation conditions

Haoda Huang[a], Qingsong Liu[e], Gregorio Iglesias[c, d], Minnan Yue[a, b, *], Weipao Miao[a, b], Qi Ye[d], Chun Li[a, b], Tingting Yang[a]

[a] *School of Energy and Power Engineering, University of Shanghai for Science and Technology, Shanghai, 200093, China*
[b] *Shanghai Key Laboratory of Multiphase Flow and Heat Transfer in Power Engineering, Shanghai 200093, China*
[c] *School of Engineering and Architecture, University College Cork, College Rd., Cork T12 K8AF, Ireland*
[d] *School of Engineering, Computing and Mathematics, University of Plymouth, Drake Circus, Plymouth PL4 8AA, United Kingdom*
[e] *Liverpool Logistics, Offshore and Marine (LOOM) Research Institute, Liverpool John Moores University, Liverpool, Byrom Street, L3 3AF, United Kingdom*

Abstract:

As shallow coastal areas for the installation of wind turbines approach saturation, wind turbines will need to be installed in deeper areas, requiring floating rather than seabed-fixed substructures. Considering factors such as economy and safety, floating offshore wind turbines (FOWTs) have become the major focus for offshore wind research and development. In the case of spar-type FOWTs, stability in the heave direction poses a challenge. With this in view, in this work a heave plate with bionic fractal structures is mounted on the bottom of the spar-type FOWT. The bionic fractal heave plates are innovatively proposed to further improve the dynamic response of the FOWT. In this study, the aero-hydro-mooring dynamic method of the FOWT is established to develop a reliable numerical solution model through the DFBI module using computational fluid dynamics software STAR-CCM+. The results of fully-coupled simulations of the original FOWT, the FOWT with heave plate (HP-FOWT) and FOWTs with 3~5-layer bionic fractal heave plate (3~5BFHP-FOWTs) are presented. Increases in average thrust and power of 0.44% and 0.99%, respectively, prove the optimal aerodynamic responses of the 5 BFHP-FOWT. As for the hydrodynamic responses, the average heave response amplitudes of the HP-FOWT and 3~5BFHP-FOWTs are significantly lower than the original FOWT. The maximum reduction (25.03%) is obtained by the 5BFHP-FOWT. The bionic fractal heave plate will slightly reduce the stability of the pitch response. For the standard deviation of the heave, surge, mooring lines 1 and 2 responses, the 5BFHP-FOWT decreases by 17.97%, 11.44%, 17.50%, and 8.25% respectively, showing the best stability improvement among the HP-FOWT and BFHP-FOWTs. Furthermore, the vortices in the bionic fractal heave plates are analyzed in detail at the Z=±0.25 m section of the flow field. Only when the specific fractal layer number is 5, the number and curl of the vortices in the fractal structure increase significantly, showing excellent effect of the energy absorption.

Keywords: Fully-coupled aero-hydro-mooring dynamics; Floating offshore wind turbine; Heave plate; Bionic fractal structure; Computational fluid dynamics

Nomenclature			
Acronyms		5BFHP-FOWT	FOWT with the 5-layer bionic fractal heave plate [-]
BEM	Blade Element Momentum [-]	***Symbols***	
BFHP	Bionic Fractal Heave Plate [-]	A_i	Response Amplitude on the Specified DOF [m]
CFD	Computational Fluid Dynamic [-]	A_n	Response Amplitude of the Decay Curve [m]
CM	Center of Mass [-]	D	Rotor Drag [N]
DFBI	Dynamic Fluid-Body Interaction [-]	d	Water Depth [m]
FOWTs	Floating Offshore Wind Turbines [-]	g	Gravity [N/kg]
IFS	Iteration Function System [-]	H_w	Wave Height [m]
ML	Mooring Line [-]	k	Turbulent Kinetic Energy [m^2/s^2]
RAO	Response Amplitude Operator [-]	L	Rotor Lift [N]
SST	Shear Stress Transport [-]	L_r	Relaxation Length [m]
SWL	Still Water Level [-]	M	Rotor Torque [N m]
TSR	Tip Speed Ratio [-]	P	Rotor Power [kW]
URANS	Unsteady Reynolds-Averaged Navier-Stokes [-]	R	The Rotor Radius [m]
VA	Victoria Amazonica [-]	R_c	Mooring Line Stiffness [N/m]
VOF	Volume of Fluid [-]	T	Rotor Thrust [kN]
6DOF	6-Degree-of-Freedom [-]	U_R	Ursell Number [-]
BFHP-FOWT	FOWT with the bionic fractal heave plate [-]	V_{hub}	Wind Speed at hub height [m/s]
BHP-FOWT	FOWT with the bottom heave plate [-]	$y+$	Dimensionless Wall Distance [-]
MHP-FOWT	FOWT with the middle heave plate [-]	λ	Tip Speed Ratio [-]
OHP-FOWT	FOWT with the original heave plate [-]	ω	Turbulent Dissipation Rate [/s]
THP-FOWT	FOWT with the top heave plate [-]	λ_m	Mass per Unit Length [kg/m]
3BFHP-FOWT	FOWT with the 3-layer bionic fractal heave plate [-]	λ_w	Wavelength [m]
4BFHP-FOWT	FOWT with the 4-layer bionic fractal heave plate [-]	ω_{rot}	Rotating Angular Velocity of Rotor [rad/s]

Corresponding author: Minnan Yue. Tel: 86 13777583803: E-mail address: ymn@usst.edu.cn

1. Introduction

In recent years, in the global effort to decarbonize the energy supply, wind energy has received increasing attention due to its advantages – it is environmentally-friendly and renewable [1]. The total installed capacity of wind turbines reached 837 MW in early 2022, a growth of 12.4% over the previous year [2]. Because of the occupation of land resources and the impact on the environment, there is a trend to shift from onshore to offshore wind turbines [3]. Compared to onshore wind energy, offshore wind energy has the advantages of not only abundant resources, but also a more uniform and stable wind speed [4]. Many shallow coastal areas where seabed-fixed wind turbines can be installed are approaching saturation – the North Sea being the clearest example. To harness wind power in deeper waters (>60 m) and further away from the coast (>30 km), it is necessary to use Floating Offshore Wind Turbines (FOWTs) [5].

At present, the platforms of FOWTs are mainly divided into four types: barge, tension leg, semi-submersible, and spar platform [6]. Compared with other platforms, the spar platform has the characteristics that the Center of Mass (CM) is far below its center of buoyancy, which provides excellent stability by generating restoring moments when the platform oscillates from its self-equilibrium position. The unique slender structure of the spar platform reduces wave loads. Resulting in good hydrodynamic performances, so that it is suitable for a variety of sea conditions [7]. Despite the above advantages, the safe and stable operation of the spar-type FOWT is still a challenge due to the interaction of the deep-sea multi-body coupling. Under the excitation of wind and wave loads, the spar-type FOWT generates 6 Degree of Freedom (6DOF) motions, which significantly affects the aerodynamic performances of the rotor, and the interaction of the wake behind the wind turbine in turn affect the stability of the platform. Moreover, the Mooring Line (ML) system is also affected by the waves, currents, and seabed conditions, resulting in constant changes in tension of the ML and stability of the platform. Therefore, in view of the complexity of the multi-body system interaction and the difficulty of realizing the Reynolds similarity criterion in laboratory tests, it is essential to perform fully-coupled simulations of the spar-type FOWT to evaluate the safety and stability of the system and provide the framework for its design optimization [8].

1.1 Solution method of the aerodynamic load

Nowadays, the traditional codes developed by Blade Element Momentum (BEM) theory, such as HAWC2, 3Dfloat, and Bladed [9], are widely used in solving the aerodynamic loads of wind turbines. Despite the high computational efficiency, the BEM method has still many limitations. One of the reasons is that the BEM method assumes the calculation process as a steady state, which is contrary to the complex and variable sea conditions of FOWT. The assumption of uniform velocity near the surface of the blades is overturned by the variation of the relative wind speed induced by the dynamic responses of the FOWT, therefore, the traditional BEM method cannot be used to solve it accurately [10].

The vortex method represents the vortex region by a set of discrete vortex particles moving in the flow region [11], and mainly solves the aerodynamic load based on the vortex model. As one of the vortex models, the free-vortex wake model is extensively applied in the research of FOWT and wake dynamics [12]. However, the fluid is assumed to be inviscid and incompressible in the vortex method, which is limited to the solution of low-speed flow. Since the free flow of vortex particles simplifies the wake motion, the vortex method cannot accurately simulate the evolution of the vortex. In addition, the selection of the vortex models and the determination of parameters require abundant experience and experimental support, which entails a considerable cost in the research of FOWTs.

With the popularity of computers and the continuous improvement of their performance, the high-fidelity Computational Fluid Dynamics (CFD) method is gradually applied in the research of the FOWT [13]. Compared with BEM method and vortex method, the computational fluid dynamics method can directly consider all the physical effects of the FOWT (viscosity, radiation effect, wave diffraction, etc. [14 -15]), and obtain detailed information about the aerodynamic load distribution of the blades and the downstream wake structure of the wind turbine through flow field visualization. It is helpful to analyze the stall process of the blades and the dynamic motion responses of the FOWT. Rezaeiha et al. [16] studied the interaction between two tandem FOWTs through the CFD tool under the surge motion conditions. The results showed that the surge motion of the upstream FOWT enhanced the wake dissipation and contributed to the recovery of the downstream wake, thus increasing the average power of the rotor. Fang et al. [17] performed the improved delayed detached eddy simulation through the CFD method to analyze the aerodynamic characteristics of the rotor and its wake distribution under surge motion. It was found that the rotor presented a light stall phenomenon under surge motion, and the wake variation caused by the surge motion of the FOWT was hard to recover. Guo et al. [18] investigated the aerodynamic characteristics of the FOWT under the surge-pitch coupling motion conditions at the same frequency and different frequencies. The results showed that the amplitudes of the power and thrust responses reached the maximum when the two motions were coupled in the same phase, leading to a sharp fluctuation of blade aerodynamic performances and fatigue damage. The above studies with regard to the FOWT are all concerned with the aerodynamic responses in a given pitch/surge motion. With the rapid development of offshore wind power, the research on real-scale aero-hydrodynamic multi-body coupling of the FOWT has received increasing attention. Oliveira et al. [19] conducted a numerical analysis of blade-tower interference of the National Renewable Engineering Lab (NREL) 5 MW FOWT by means of the CFD software. A reliable solution model was established by numerical verification, and the distribution law of the wake was analyzed through flow field visualization. Quallen et al. [20] modelled a fully-coupled system for solving the FOWT considering wind and wave loads. Compared to the results obtained by NREL, the maximum surge response of the proposed model showed a 13.8% decrease, while the minimum surge response presented a 10.9% decrease. Liu et al. [21] used OpenFoam software to develop the numerical calculation of the real-scale FOWT under different operating conditions. The mutual influence of the wind turbine, platform, and mooring system was quantitatively analyzed on the basis of the flow field and response results, thus providing a theoretical reference for the study of three-dimensional fluid-structure interaction.

1.2 Stability improvement methods of the spar-type FOWT

In practical applications, the stability in heave motion under wave excitation conditions poses a challenge for the spar-type FOWT, with the potential for large motions to result in fatigue or even damage of the moorings and structures. Therefore, how to improve the stability in heave motion of the spar-type FOWT has become an objective in marine engineering research. There are two main methods to improve – to increase the draft of the platform, and to enhance the additional mass and damping of the platform through plate-like appendages [22]. The later method, i.e., the plate-like appendage or "heave plate", is widely applied for its advantages of low cost, convenient installation, and additional hydrodynamic damping. Hegde et al. [23] studied the influence of different heave plate positions on the hydrodynamic performance of a spar platform by a combination of experiments and simulations. Compared with the original spar platform, a 75% decrease was found in the heave response peak and a 30% decrease in the pitch response peak when the heave plate is near the top of the platform. Rao et al. [24] studied the damping in heave direction of a scaled spar platform model installed with heave plates subjected to the given heave motions at different frequency-amplitude combinations. It was found that the damping in heave direction enhanced significantly when the heave plate is at keel, with damping levels 10 times higher at lower motion amplitudes and 5 times higher at higher amplitudes. Subbulakshmi et al. [25] used the WAMIT software to analyze the influence of viscous damping on heave response of a single/double heave plate spar platform. It was concluded that the heave response of spar platform can be improved when the diameter of the heave plate and the distance between the two heave plates increase.

In summary, heave plates are effectively in improving hydrodynamic performance of the spar platform. However, most of the current studies focus on the influence of the external factors of the heave plate, such as number, size, position, etc. In view of the relatively few studies on the heave plate itself, a heave plate with better performance structure should be proposed to further improve the stability of the spar-type FOWT. Therefore, this study proposed a heave plate with bionic fractal structure applied to spar-type FOWT, and used the established numerical model to calculate the effect of this structure on the stability of FOWT.

1.3 Survey of bionic fractal methods

The adaptation of organisms in nature to the environment is ubiquitous, which is not only reflected in their physiology and behavior, but also in the morphology and structure. As shown in Fig. 1(a)~(b), the surface of the leaves of plants has many tiny pores and small capillaries, which can effectively transport water and maintain high water content [26]. The control surface of the fin-shaped limb of the minke whale is small and narrow, which plays an important role in maintaining the positive pitching body direction during different types of feeding movements [27]. Furthermore, the periodic topological structure of the honeycomb enables it to effectively absorb energy shocks[28], shown in Fig. 1(c). It can be seen from the above that biological structures have excellent mechanical and hydrodynamic properties. Therefore, designing a light weight, high performance and even multi-functional structure through bionic methods has become a development trend [29]. Inspired by the microstructure of bamboo, Fu et al. [30] proposed 6 bionic pipes with different cross sections, and analyzed their energy absorption effects by LS-DYNA software. It was observed that the energy absorption effect of the bionic-bamboo tube was better than that of a bare bitubal circular tube due to the interaction between rib and tube wall. In order to reduce the loss caused by the train impact accident, Peng et al. [31] compared the performance of the two structures of neuron bifurcation branch structures and bionic dendritic furcal structures by numerical method. It was reported that the dendritic branch structure with six ribs and third-order parting has the best anti-collision effect under the operating condition of 10 m / s, a 16.18% increase in specific energy absorption compared with original one. Wang et al. [32] designed a new bionic collision box with human tibia as the object. It was found that the new bionic collision box has excellent energy absorption performance and more stable collision process than the original collision box. As an aquatic plant, Victoria Amazonica (VA) has excellent hydrodynamic characteristics, which benefits from the crisscross branch structure at the bottom of the leaves. Under severe water conditions, the cavity structure at the bottom of VA can effectively dissipate energy, while the air in the branch structure further improves the buoyancy. In view of the excellent structural characteristics of the leaf-vein branch of VA, it has a large number of bionic applications in architecture, such as support structure and roof design [33], Fig. 1(d). For the mechanical properties of the leaf-vein-like branch structure, some scholars have also made relevant research. Inspired by the ribs of the VA, Zhao et al. [34] redesigned the original parallel stiffening ribs on the inner side of the beam to be distributed according to the leaf-vein pattern of VA. The specific stiffness and the maximum static deformation of the VA structure showed a 17.36% increase and a 16.22% decrease compared with the original structure. By imitating the leaf-vein branch structure of the lotus leaf of the same family as VA, He et al [35] proposed a new type of circular tube as an efficient energy absorber. The numerical results indicated that when the main vein branch is 6 and the ratio of inner and outer diameter of the circular tube is 0.5 ~ 0.7, the leaf-vein branch structure has better energy absorption effect. Therefore, it is feasible to improve the energy absorption properties of the structure through the bionic leaf-vein branch distribution mode of VA, which lays a foundation for subsequent research.

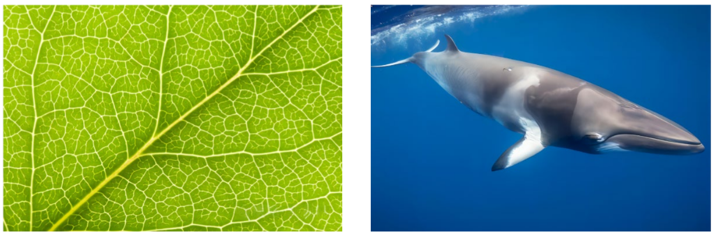

(a) Leaf vein (b) Sponge

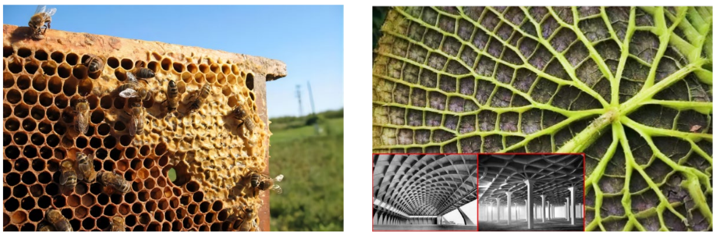

(c) Honeycomb (d) Victoria Amazonica

Fig. 1. Different types of biological structures.

Although the vein distribution of each VA is different, each part follows the same growth pattern, which is the fractal structure. The inherent law of the fractal structure is self-similarity [36], in other words, the shape of each part of the fractal body is the approximation of the overall scale, such as nerves, branches, even coastlines. Since Mandelbrot [37] put forward the concept of fractal theory, it has been the object of much research. Wang et al. [38] expanded the research of Koch fractal structures with different fractal orders through experiments and numerical simulations. The results indicated the Koch fractal order has a significant influence on the energy absorption efficiency. Through the interaction with the outer wall, the Koch fractal structure dissipated more collision energy than the original one, and the second-order fractal structure has the best energy absorption effect. Li et al. [39] investigated the compression behavior of fractal honeycomb structures with different array structures by theoretical and numerical simulation. Compared to the original honeycomb structure, the specific energy absorption of the proposed triangular, square, and hexagonal fractal honeycomb structures was increased by 85 %, 110 % and 95 %, respectively. Altogether, the fractal structure enhances the energy dissipation rate and reduces the fatigue load, to protect the structure [40]. Obviously, the unique random fractal structure of VA also has the above characteristics. In a sense, any system tends to release energy to its surrounding environment to increase the entropy of the whole system. In the random fractal structure, due to its complex fractal morphology and nonlinear dynamic behavior, its energy absorption mechanism is also more complex. The energy is dispersed into the whole system through the branch and bifurcation structure, thereby increasing the entropy of the system and making the system more stable. At the same time, the self-similarity of the fractal structure also makes the energy distribution more uniform, further increasing the entropy of the system. On these grounds, this paper proposes a Bionic Fractal Heave Plate (BFHP) based on VA to improve the heave response of the FOWT.

1.4 Primary work

In this study, the fully-coupled calculation of the NREL 5 MW spar-type FOWT was performed by means of CFD software STAR-CCM+. The dynamic responses of the FOWT were achieved by the superposition motion and Dynamic Fluid-Body Interaction (DFBI) modules, and the multiphase flow was established through the Volume of Fluid (VOF) method. In this paper, the main elements of the work are:

(1) The reliability of each coupling part of the FOWT was verified under the present CFD method. Firstly, the aerodynamic performance was verified by calculating the thrust and power of the rotor at different wind speeds. Secondly, the results of free decay tests and aero-hydrodynamic response under single regular wave/wind excitation were compared with other code results. Eventually, the aero-hydrodynamic performance of the fully-coupled FOWT was analyzed with the wind and wave loads.

(2) The hydrodynamic response of the FOWT with three different installation positions of the heave plate was compared under the regular wave only condition. The optimal installation position of the heave plate was selected to carry out the fully-coupled simulation of the original FOWT, FOWT with the original heave plate, and FOWTs with the BFHP. And the effects of the BFHPs with different fractal layers on the dynamic response of the FOWT were further compared.

(3) The distribution of flow field in BFHP was studied by the visualization results. The complex interaction of the FOWT wake was analyzed through three-dimensional instantaneous iso-parametric contours. The bi-dimensional cut

at the Z=0.25 m section was presented to investigate the vortex development in the branch structures.

The reliable FOWT model established in this paper lays the foundation for the subsequent flow field optimization design. At the same time, the proposed bionic fractal method has theoretical reference value for the safe and reliable operation of FOWT.

2. Model establishment

In this section, the specific parameters of the real-scale FOWT are presented in subsection 2.1. The multibody coupled motion of the FOWT with wind and wave loads are shown in subsection 2.2. The BFHP is proposed and modelled in subsection 2.3 and the main analysis parameters are defined in subsection 2.4.

2.1 Spar-type FOWT model

The NREL 5 MW wind turbine mounted by the spar platform in Code Comparison Collaboration (OC3) - Phase IV project is used to carry out the fully-coupled simulations [41], Fig. 2. The overall system of the FOWT consists of rotor, tower, nacelle, platform, and MLs. Here, the maximum and minimum diameters of the spar platform are 9.4 m and 6.5 m, while the CM of the real-scale platform and fully-coupled FOWT are 89.9155 m and 78.04 m below the Still Water Level (SWL). More specifically, Table 1 summarizes the specific parameters of each coupling part. Table 2 generalizes the ML system parameters [41]-[42]. And the parameters of the real-scale FOWT measured by modeling software NX 12.0 are generalized in Table 3.

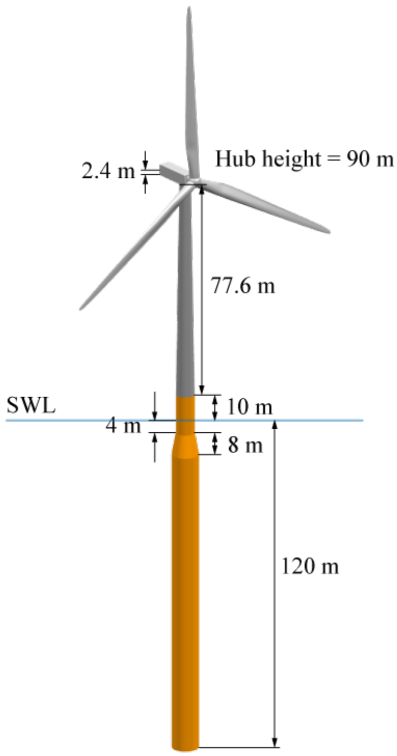

Fig. 2. Spar-type FOWT model.

Table 1
Specific parameters of each coupling part of the FOWT.

Properties (relative to SWL)	Value
Rated wind speed	11.4 m/s
Rated rotor speed	12.1 rpm
Rotor mass	110,000 kg

Nacelle mass	240,000 kg
Tower mass	347,460 kg
Rotor diameter	126 m
Hub diameter	3 m
Platform mass	7,466,330 kg
Platform CM position	89.9155 m
Roll inertia	4.229×10^9 kg m^2
Pitch inertia	4.229×10^9 kg m^2
Yaw inertia	1.642×10^8 kg m^2

Table 2

Specific parameters of ML system.

Properties of ML system (relative to SWL)	Value
Angle between adjacent ML	120°
Fairleads, anchors depth	70 m, 320 m
Fairleads, anchors radius	5.2 m, 853.87 m
Unstretched length of MLs	902.2 m
Anchors radius	853.87 m
Equivalent density of MLs	77.7066 kg/m
Equivalent extensional stiffness	384,243,000 N/m

Table 3

Specific parameters of real-scale FOWT.

Properties of platform (relative to SWL)	Value
Gross mass	8,066,000 kg
CM position	78.04 m
Roll inertia	2.0×10^{10} kg m^2
Pitch inertia	2.0×10^{10} kg m^2
Yaw inertia	1.642×10^8 kg m^2

2.2 Motion description

The multi-body coupling system of the FOWT interacts with each other, making its motion responses complicated and changeable. Fig. 3 presents the multibody coupled motion of the FOWT with wind and wave loads. As shown in Fig. 3, the coupling parts of FOWT interact with each other under wind and wave loads, resulting in complex 6DOF (heave, surge, sway, pitch, roll, and yaw) motions. The existence of the MLs (ML1, ML2, and ML3) system effectively improves the 6DOF motion of the platform and enables the FOWT to operate stably. However, when the wind load is considered, the stable position of the surge response of the platform will shift to the windward direction, which is bound to aggravate the fatigue damage of MLs. In addition, the interaction between the aerodynamic and hydrodynamic responses cannot be ignored. For these reasons, the FOWT generates complex dynamic responses, which are hard to predict.

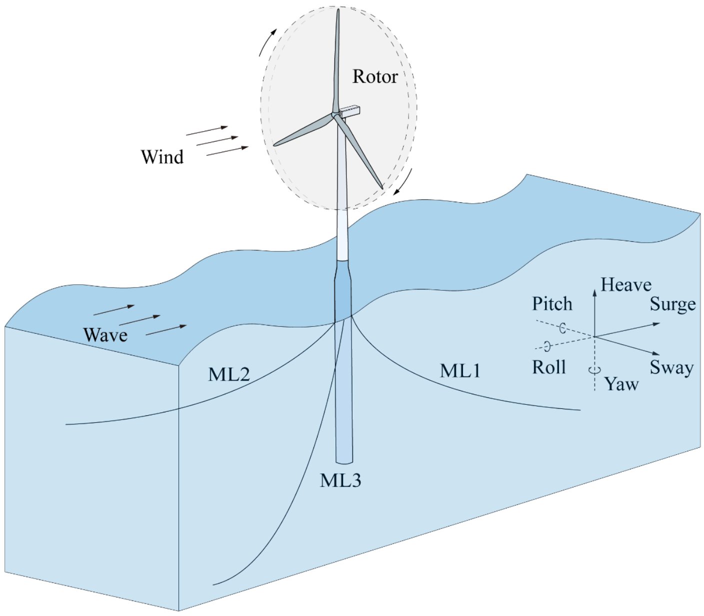

Fig. 3. Multi-body coupled motion of FOWT.

2.3 Modeling of the BFHP

In this study, the proposed BFHP was established based on the branch structure of VA. The bionic fractal structure not only has different scale change rules, but also has discontinuous and non-differentiable problems in space, which brings difficulties in solving geometric nonlinearity and multi-scale physical fields in numerical simulation. Therefore, based on the IFS (Iteration Function System) of fractal geometry, this study obtains the parametric model of the fractal structure by using the conceptual design tools of topology optimization, shape optimization, and size optimization. The parametric modeling method of VA is shown in Fig. 4. In Fig. 4(a), the modeling process of the branch structure is presented in 6 steps: (1) construct the concentric circle series; (2) generate the regular distribution points through a mathematical expression describing the geometric characteristics of VA, expressed as eqn. 1; (3) reconstruct the random distribution points to describe the random characteristic of VA; (4) generate the branch structure in a network of curves by calculating the shortest path of each point between concentric circles; (5) remove the concentric circle to obtain the original branch structure; (6) smooth the branch nodes by curve smoothing algorithm. Fig. 4(b) presents the advantage of parametric modeling, that is, the multi-level branch structure can be obtained by changing the number of concentric circles. The ribs are equidistantly modeled around the concentric circle in Fig. 4(c). To present the characteristics of random fractal structure, the shape and size of the original leaf-vein branch structure are optimized, and the VA parametric model is finally obtained.

$$n_x = y \cdot x \cdot 2 - 2 \text{ , } (x = 1, 2, 3, \ldots) \tag{1}$$

where n_x is the number of points on the xth concentric circle from inside to outside; y is a given value, 5.

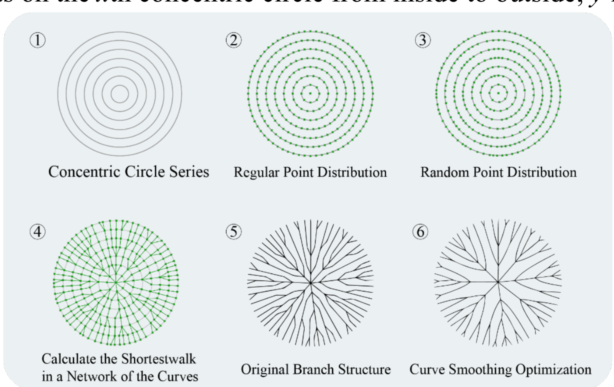

(a) Modeling of the leaf-vein branches

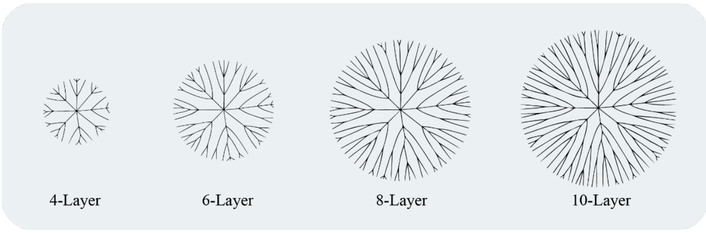

(b) Multilevel branch structure

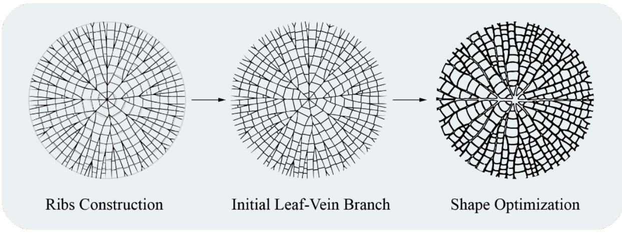

(c) Rib modeling and shape optimization

Fig. 4. The parametric modeling process of VA.

The BFHP is installed at the bottom of spar platform, with the diameter and thickness of 18.8 m and 1 m (Fig. 5). The BFHP is achieved by means of Boolean operation of the original heave plate and VA vein parametric model, in which the thickness of the fractal cavity structure is 0.5 m. For the research of the influence of fractal dimension on the stability enhancement effect of heave plate, the 3-layer, 4-layer and 5-layer fractal heave plates are finally established by scaling the VA vein parametric model. In this study, the DFBI model is used to simulate the force and motion of a rigid body in a fluid environment. Therefore, the material properties of the proposed BFHP are not considered, and it is regarded as a rigid body integrated with the whole wind turbine. The density of the BFHP is 893 kg/m^3, which is consistent with the average density of the spar platform.

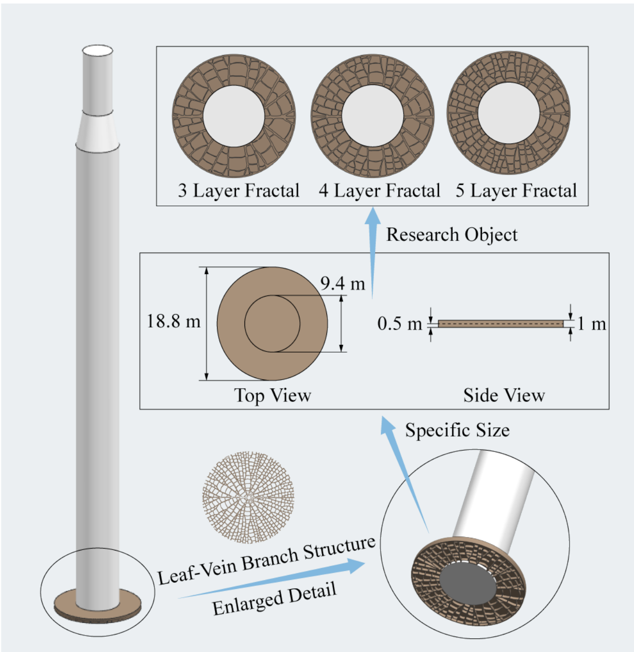

Fig. 5. Spar platform with the BFHP.

2.4 Definition of parameters

The Tip Speed Ratio (TSR) intuitively reflects the blade rotation speed, which can be defined as the ratio of the blade tip linear speed to the wind speed at the hub height, shown as [43]:

$$\lambda = \frac{\omega_{\text{rot}} \cdot R}{V_{\text{hub}}} \tag{2}$$

where the ω_{rot} is the angular velocity of the rotor; V_{hub} is the wind speed at hub height; R is the rotor radius.

Thrust (T) and power (P) are the main parameters to reflect the aerodynamic performances of the FOWT. The thrust is defined as the component of the resultant force in horizontal direction on the rotor, and the power is the product of the torque and angular velocity on the rotor, specifically defined as [44]-[45]:

$$T = L\cos\alpha + D\sin\alpha \tag{3}$$

$$P = M \cdot \omega_{\text{rot}} \tag{4}$$

where L is the rotor lift; D is the rotor drag; M is the rotor torque; α is the angle between the relative velocity and the windward surface of rotor.

The Response Amplitude Operator (RAO) is an important parameter to describe the response characteristics of the marine structure under wave excitation, which is expressed as the ratio of response amplitude to height of the wave under unit wave height excitation. Through the research and analysis of RAO, the response characteristics of marine structures are predicted more accurately, providing the reference for the design and safety assessment of marine engineering. It can be expressed as [46]:

$$\text{RAO} = A_i / H_w \tag{5}$$

where the A_i represents the response amplitude of the structure on the specified DOF; H_w is the wave height.

The logarithmic decrement is commonly used to measure the damping ratio of the offshore structure, defined as:

$$\delta = \frac{1}{n}\ln\frac{A_n}{A_{n+1}} \tag{6}$$

where A_n represents the nth responses amplitude of the decay curve.

The damping ratio describes characterize the modal damping of the structure, which reveals the energy dissipation intensity of the structure during the oscillation process, expressed as [47]:

$$\xi_d = \frac{\delta_d}{2\pi} = \frac{1}{2\pi}\cdot\frac{1}{n}\ln\frac{A_n}{A_{n+1}} \tag{7}$$

where the δ_d is the logarithmic decrement; A_n is the response amplitude of the nth decay period.

3 Solution model

This section introduces the model required for the fully-coupled simulation. In subsection 3.1, the SST k-ω model is introduced to calculate the turbulence. The VOF and DFBI models are described in subsections 3.2-3.3. Lastly, the ML system of the FOWT is defined in subsection 3.4.

3.1 Governing equation

The Reynolds-Averaged Navier-Stokes (RANS) method regards the turbulent flow process as the superposition of the average flow and instantaneous pulsation of the fluid in a certain time scale by the time averaging method, presenting high accuracy and good robustness while greatly reducing the requirements for computing resources. When solving unsteady flow, it is also called URANS method. The common turbulence models of RANS method include k-ε model, k-ω model and Shear Stress Transport (SST) k-ω model. Compared with previous two models, the SST k-ω model (adopted in this study) has the same advantages as the k-ε model and can accurately simulate the near-wall boundary layer and the far-field free flow region. The basic equation is as follows:

$$\frac{\partial(\rho k)}{\partial t} + \frac{\partial(\rho u_p k)}{\partial x_p} = \frac{\partial}{\partial x_q}(\Gamma_k \frac{\partial k}{\partial x_q}) + G_k - Y_k + S_k \tag{8}$$

$$\frac{\partial(\rho \omega)}{\partial t} + \frac{\partial(\rho u_p \omega)}{\partial x_p} = \frac{\partial}{\partial x_q}(\Gamma_\omega \frac{\partial \omega}{\partial x_q}) + G_\omega - Y_\omega + D_\omega + S_\omega \tag{9}$$

where k represents the turbulent kinetic energy; ω is the turbulent dissipation rate; Y_k and Y_ω represent the dissipation terms induced by turbulent; Γ_k and Γ_ω denote the effective diffusivity term induced by turbulence; D_ω is the term of transverse dissipative derivative; S_k and S_ω are custom source terms; p and q indicate Einstein Summation Convention.

3.2 Wave model

In this study, the VOF wave model is established to realize the propagation and deformation of waves in complex seabed topography. It is based on the concept of Volume of Fluid, separating the fluid and non-fluid regions, so that the movement of the fluid surface can be accurately tracked. The transport equation is shown as:

$$\frac{\partial n}{\partial t}+\nabla\cdot\left[\left(\mathbf{U}-\mathbf{U}_{\mathrm{g}}\right)n\right]+\nabla\cdot\left[\mathbf{U}_{\mathrm{r}}\left(1-n\right)n\right]=0 \tag{10}$$

where $\mathbf{U}$, $\mathbf{U}_{\mathrm{g}}$, and $\mathbf{U}_{\mathrm{r}}$ are the three-dimensional vectors, which represent wave propagation velocity, mesh moving velocity and compression term of velocity field, respectively; n defines the proportion of air-water phase in the computational domain.

For deeper waters, the steady-state waves can be modeled by Stokes theory. As one of the wave models, the fifth-order Stokes wave [48] is closer to the real wave than the first-order one. Generally, the validity of the Stokes wave model is judged by the Ursell number (applicable when less than 30), as follows:

$$U_R=\frac{H_w\lambda_w^{\ 2}}{d^3} \tag{11}$$

where λ_w is the wavelength; d is the water depth.

3.3 DFBI model

The DFBI model has a wide range of applications, which can be used to simulate the motion and force of rigid bodies such as wind turbines, automobiles, and ships, and provide effective tools for product design and optimization. By calculating the trajectory of the rigid body through DFBI method, the force and motion of the rigid body in the fluid environment can be predicted more accurately. The specific process of the fully-coupled solution to the FOWT (regarded as rigid body in this study) through DFBI model is shown in Fig. 6.

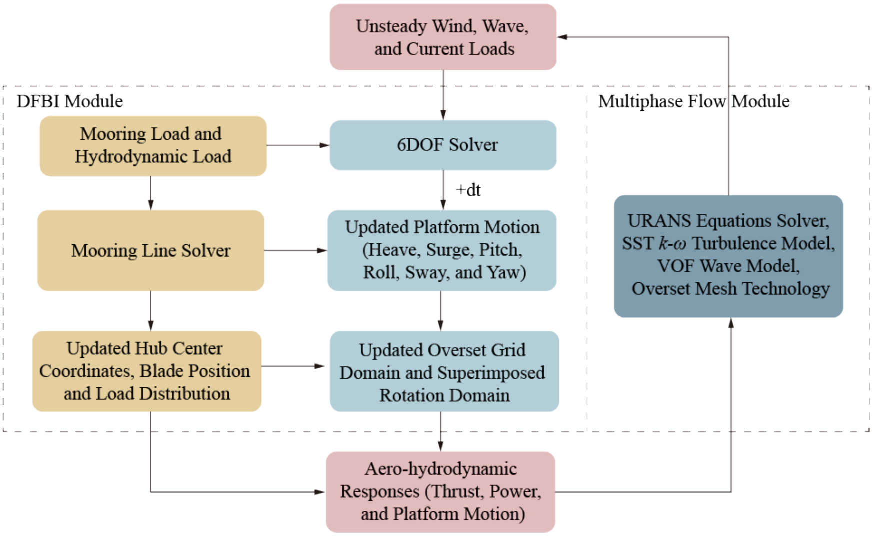

Fig. 6. The fully-coupled calculation process of FOWT

3.4 Catenary system

Based on Newton 's Second Law and Principle Virtual Work, the hydrostatic equilibrium state and dynamic response of the catenary system are calculated under the gravity and fluid force. This model can accurately simulate the movement and force of the system, including catenary tension, wind load, and wave load. The catenary shape in

Cartesian coordinates is defined as:

$$\begin{cases} x = a_1 m + a_2 \sinh(m) + \alpha \\ y = a_1 \cosh(m) + \dfrac{a_2}{2} \sinh^2(m) + \beta \\ m_1 \le m \le m_2 \end{cases} \tag{12}$$

where α and β are the integral constants; m is the curve parameter; m_1 and m_2 denote the position of the catenary anchor point; a_1 and a_2 are defined as:

$$\begin{cases} a_1 = \dfrac{a_3}{\lambda_m g} \\ a_2 = \dfrac{a_3 a_1}{R_c L_r} \\ a_3 = \dfrac{\lambda_m L_r g}{\sinh(m_2) - \sinh(m_1)} \end{cases} \tag{13}$$

where g is the gravity; λ_m is the mass of catenary per unit length; L_r represents the relaxation length; R_c denotes the stiffness.

The forces F_1 and F_2 imposed on the ends of the catenaries follow the local tangent vector directions of the catenary curve at the values of m_1 and m_2, respectively, which are expressed as:

$$\begin{cases} F_{1,x} = a_3 \\ F_{1,y} = a_3 \sinh(m_1) \\ F_{2,x} = -a_3 \\ F_{2,y} = -a_3 \sinh(m_2) \end{cases} \tag{14}$$

From Eq. (12), it is seen that F_1 and F_2 are tangent to the catenary curve with equivalent horizontal components but opposite symbol. For the coupling between the body and the environment, such as the condition of the FOWT, the catenary system is shown in Fig. 7.

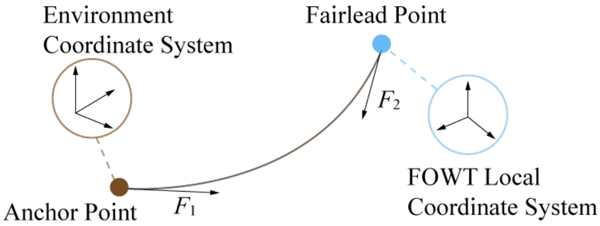

Fig. 7. ML system of the FOWT

4 Numerical model

This section presents the boundary conditions (subsection 4.1) and mesh division (subsection 4.2) of the FOWT calculation domain in detail. Then, the mesh independence verification is carried out in subsection 4.3.

4.1 Boundary conditions

The multi-physics coupling model of the real-scale FOWT was established by DFBI method in final. The whole cuboid domain is modelled as 1200(X) × 400(Y) × 593(Z) (Fig. 8). The free surface is modelled by means of the VOF method, where the depth below the SWL is 320 m, and the height above the SWL is 273 m. Combined with Fig. 8(a)~(c), the FOWT is 300 m and 900 m from the velocity inlet and pressure outlet boundaries perpendicular to the X axis direction, respectively. The two symmetrical planes perpendicular to the Y axis are 200 m away from the FOWT. In addition, the anchor of the ML system is located outside the flow field. To consider the buoyancy influence of the ML, the equivalent density of the ML is set to 70 kg/m in this study. The specific anchoring parameters are presented in Fig.8 (b)~(c).

The wave damping was set at one wavelength (λ_w=158 m) distance from the outlet boundary. This setting effectively dissipates the wave oscillations in the vicinity of the outlet, thus preventing far-field wave reflections from affecting the FOWT. Most of the cases studied in this paper were carried out at the rated wind speed (11.4 m/s). The wave height was defined as 6 m, with the wave period T_w of 10 s. The rotor speed was 12.1 rpm under the wind speed of 11.4 m/s. When the simulation performs, the FOWT does not immediately produce motion, but begins to release motion after the flow field is stabilized. The time taken for this process is the release time, which is generally 10 to 50 times the time step. In this study, the release time was 0.5 s. In the early stage of the simulation, there is a violent fluctuation in the flow field, which will adversely affect the simulation results. By setting the buffer time, the flow field is gradually stabilized and the influence of fluctuation on the simulation results is reduced. The buffer time was defined as 5 s in this study, about 10 times the release time. The density of the water and the air were 1025 kg/m^3 and 1.225 kg/m^3, respectively. Compared with the first-order Stokes wave, the fifth-order Stokes wave has higher calculation precision and more accurate wave prediction effect, and thus meets better the needs of complex marine engineering and marine environmental problems. Therefore, the fifth-order Stokes wave was adopted in this study.

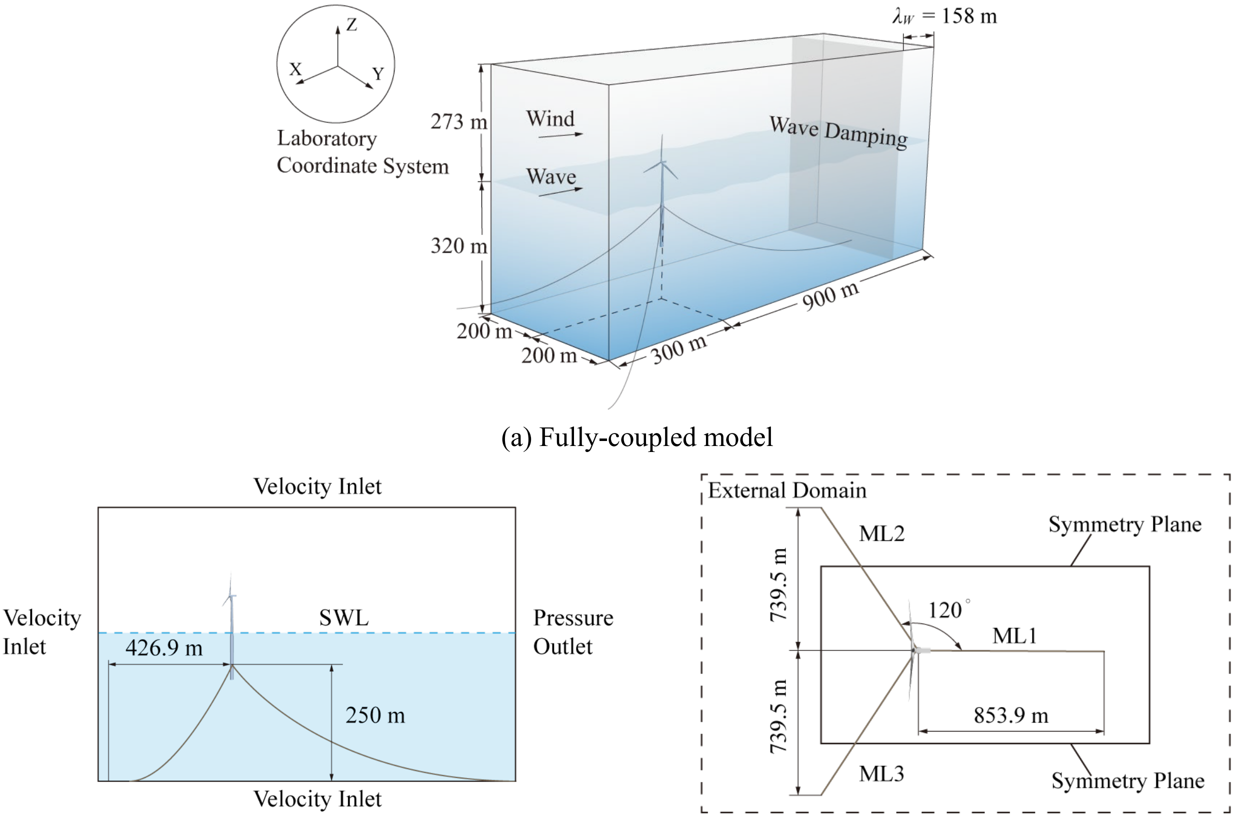

(a) Fully-coupled model

(b) Front view

(c) Top view

Fig. 8. Boundary conditions of the domain.

4.2 Mesh division

For large-scale simulation, the trimmed mesh has a high share in the unit volume, which can reduce the number of generated grids and effectively reduce the numerical divergence. For complex surfaces, the trimmed mesh can also generate high precision mesh efficiently. Thus, the trimmed mesh generator was adopted to divide the whole domain mesh. The mesh scene of the calculation domain is presented in Fig. 9. The overall mesh distribution of the domain is observed in Fig. 9(a) with details at the hub and nacelle. The mesh division at bottom of the spar platform with BFHPs is shown in Fig. 9(b), where the mesh quality at the bottom of the three different BFHPs (3-layer, 4-layer, and 5-layer) is displayed. The 2D cut at Y=0 in Fig. 9(c) is to present the mesh distribution of the calculation domain and dynamic mesh technology more clearly. It is seen from the 2D section that the domain mesh is mainly divided into three parts, including flow field, 6DOF motion region, and rotation region. The flow field is composed of gas-water two-phase flow, where there is the wave refined at the interface and the wake refined after the rotor. The wave refined requires no less than 20 layer meshes in the direction of the wave height, and no less than 80 layers in a wavelength in the direction of the wave advance [49]. And the wake refined is critical to ensure the accurate capture of the flow characteristics. Moreover, the volume control plays a transitional role of the mesh between the flow field and the overset region. The overset mesh technology is used to achieve the 6DOF motion of platform, while the blade rotation is realized through the sliding mesh technology with superimposed motion. For the purpose of accurately capturing the flow field characteristics near the boundary layer, 16 layers of prism mesh are generated near the wall, of which the thickness of the first layer is 8×10^{-4} m. By monitoring the $y+$ value of the fully-coupled system, it is seen that the maximum $y+$ at the tip of the blade is about 100, while the maximum $y+$ of the whole system is approximately 220. Based on the above setting, the number of the global meshes of the FOWT with 3~5-layer BFHP structures (3BFHP-FOWT, 4BFHP-FOWT, and 5BFHP-FOWT) is 10,441,808, 10,464,323, and 10,582,198, of which the mesh number in overset region is 2,584,418, 2,604,970, and 2,726,413, respectively. The number of rotating domain and flow field grid is basically the same.

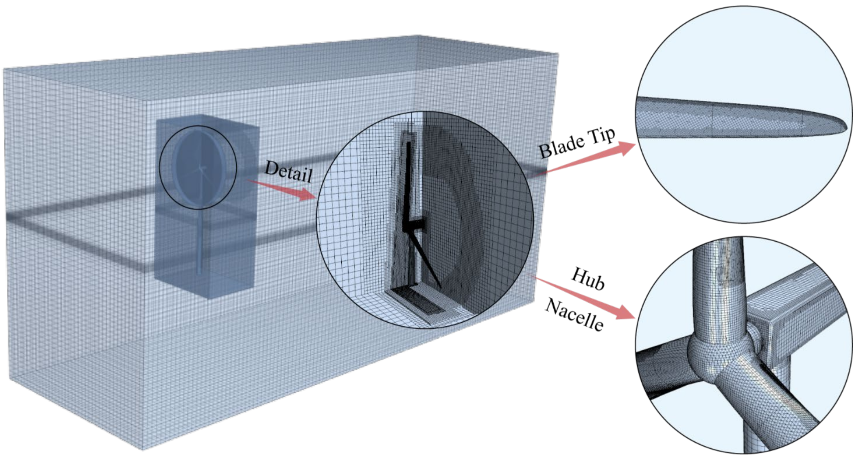

(a) Domain with details

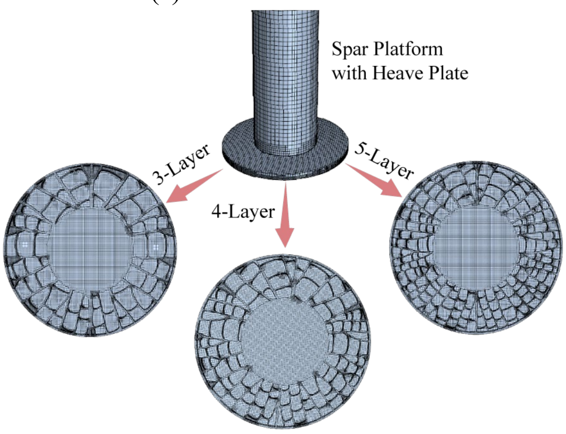

(b) Fractal heave plate

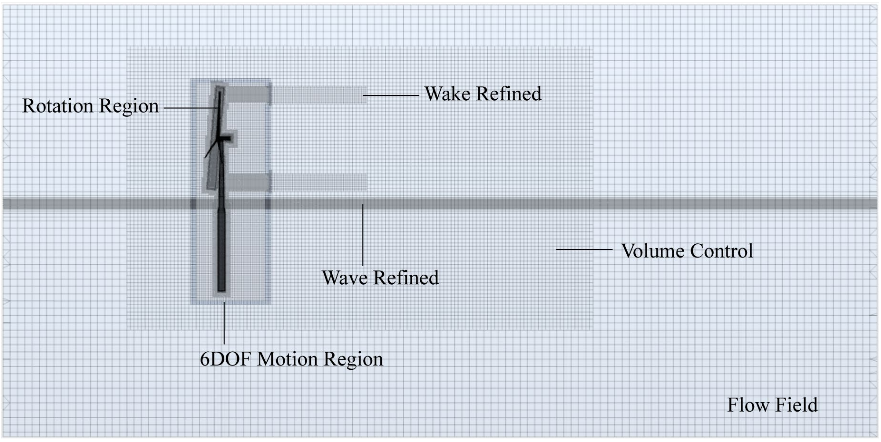

(c) 2D cut at Y=0

Fig. 9. Mesh division of the FOWT with bionic fractal heave plates.

4.3 Mesh independence verification of the aero-hydrodynamic performance

The mesh independence of the aerodynamic part was verified to determine a reasonable number of the mesh for subsequent calculations. Three cases of 4.35 million, 6.54 million and 8.53 million meshes were selected and calculated to 100 s. The time step of 0.02755 s corresponded to the time required for each rotation of the blade by 2 deg. Eventually, the average power in the three periods after stability was compared. The -1.02% minimum deviation indicated that the aerodynamic performance was mesh independent, which is shown in Fig. 10(a). In consequence, within an acceptable range, this study adopted the 6.54 million meshes for subsequent research to save the calculation source.

The hydrodynamic mesh independence was verified through modelling only spar platform. A total of 1.26 million, 2.31 million, and 3,30 million meshes respectively were calculated under the regular wave conditions. The total calculation time was 1000 s, and the pitch amplitude in the last three response periods was compared, as shown in Fig. 10(b). The 2.21% maximum deviation proves that the pitch response was mesh independent. Thus, this paper chooses the mesh number of 2.31 million to carry out the subsequent calculation.

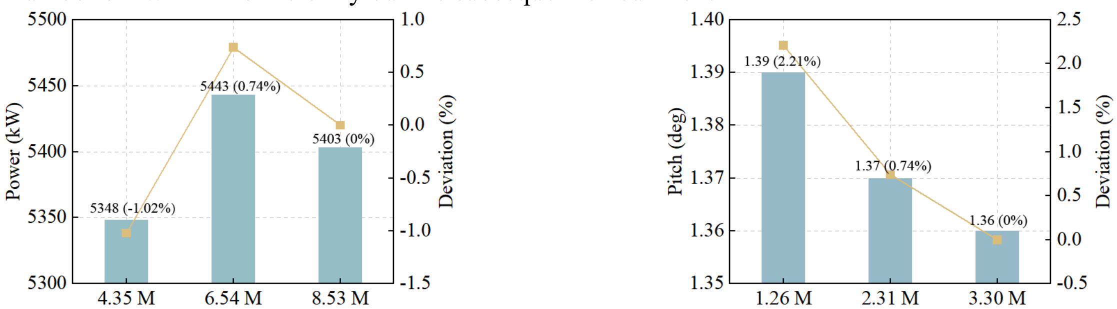

(a) Aerodynamic performance (b) hydrodynamic performance

Fig. 10. Mesh independence verification of aero-hydrodynamic performance.

The mesh independence verification of the hydrodynamic performance of the BFHP structures was carried out considering the spar platform and the 5BFHP structure. The whole domain meshes were divided according to the basic sizes of 8m, 10m and 12m respectively. The final number of meshes are 2.47 million, 4.33 million and 5.86 million in the whole domain, respectively, whereas the meshes in the overset domain are 1.92 million, 2.73 million, and 3.47 million. The average heave amplitudes in the last three periods are shown in Fig. 11. The 4.12% maximum deviation shows that the heave response was mesh independent. The mesh number of 4.33 million is enough to accurately calculate the hydrodynamic responses of BFHP structures. Therefore, the 10 m basic mesh size was selected to mesh all the BFHP structures.

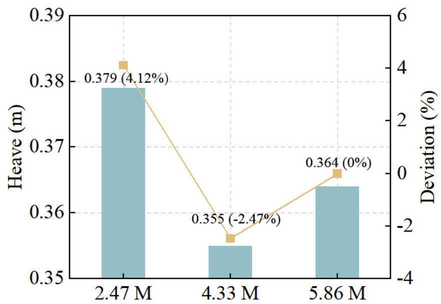

Fig. 11. Mesh independence verification of 5BFHP structure.

5 Reliability verification of the FOWT numerical model

In this section, the aero-hydrodynamic verification is presented in subsection 5.1. The influence of the heave plate position on the hydrodynamic performance of the FOWT is studied in subsection 5.2. Subsection 5.3 presents the system natural properties of the BFHP-FOWTs. Table 4 summarizes the specific setting details of each case.

Table 4

Summary of the cases calculated in this section.

Cases	Enabled	Wind Loads	Wave Loads	Analysis Type
1	Rotor	V_{hub}=11.4 m/s	None	Aerodynamic verification
2	Platform	None	None	Free decay test
3	Platform, tower	None	Regular Wave, H_w=6 m, T_w=10 s	Hydrodynamic responses
4	Platform, tower, rotor	Steady, uniform, V_{hub}=8 m/s	None	Aero-hydrodynamic responses
5	Platform	None	None	Free decay test of HP-FOWTs
6	Platform, tower	None	Regular Wave, H_w=6 m, T_w=10 s	Hydrodynamic responses of HP-FOWTs
7	Platform	None	None	Free decay test of BFHP-FOWTs

5.1 Aero-hydrodynamic performance verification of the original FOWT

(i) Aerodynamic performance verification

Cases 1 consisted in the aerodynamic reliability verification of the rotor under the rated wind speed conditions with wind shear index of 0.12. It is readily seen in the results (Fig. 12) that the thrust and power calculated by the present CFD method in this study present a certain deviation with the FAST_BEM results [50] at low wind speed. However, the results obtained by the CFD method are generally consistent with those obtained by the FAST code as the wind speed increases. Therefore, the present CFD method to solve the aerodynamic load ensures good accuracy in the wind speed range calculated in this study.

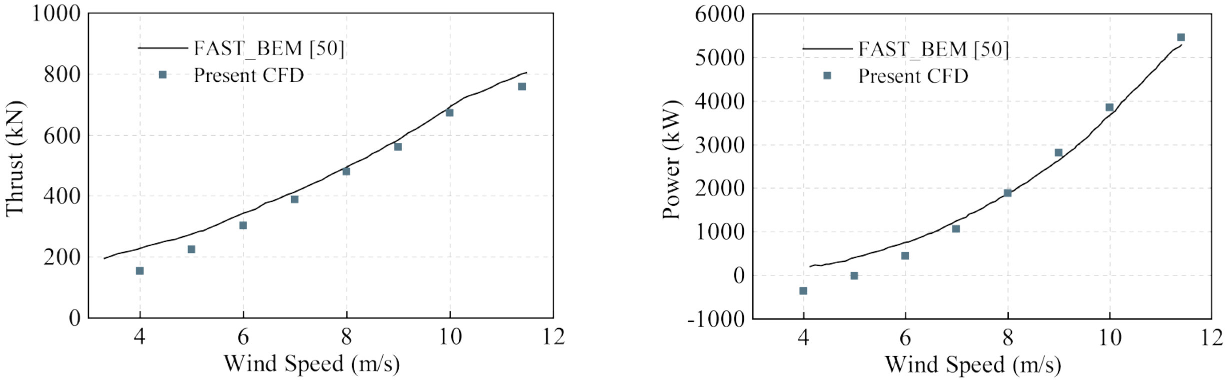

(a) Thrust (b) Power

Fig. 12. Verification of the aerodynamic performances.

(ii) Free decay test

The free decay test of the floating body is an important method to evaluate the motion response and stability of marine engineering structures in marine environment, which can effectively verify the reliability and safety of the offshore structures. In this study, only the platform was modeled to perform the free decay test due to the rotor is in a static state; however, the gross mass of the FOWT system should be considered. Case 2 calculated the free decay responses under the still water condition, and the results are compared with several codes [51] (Fig. 13). It is readily seen that the surge response calculated by the present CFD method is consistent quite well with the FAST code, while the logarithmic decrement presents differences with the ADAMS and HAWC2 codes. The pitch response shows excellent agreement with the ADAMS code; however, with the passage of time, the difference with the HAWC2 and FAST codes gradually becomes significant. Since the viscous effect of the fluid is considered, although the results are different, they are within a reasonable range. Table 5 summarizes the free decay period of the surge, pitch, and heave responses. The great consistency with other codes shows that the present CFD method is reliable.

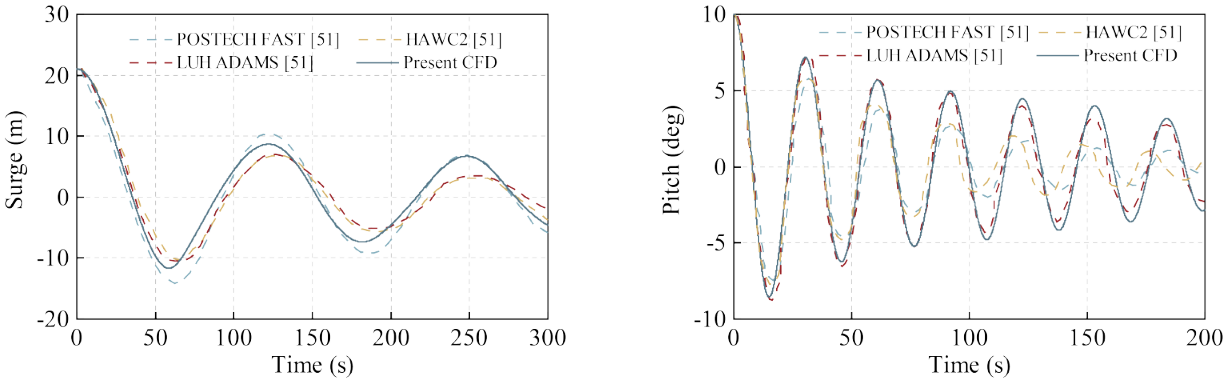

(a) Surge (b) Pitch

Fig. 13. Verification of the free decay test.

Table 5

Free decay period comparison among present CFD method and other codes.

Cases	DOF	POSTECHFAST [51]	HAWC [51]	LUH ADAMS [51]	Present CFD
2	Surge	123.8	130.0	124.0	122.2
	Pitch	31.6	31.3	31.7	30.3
	Heave	31.0	34.4	31.3	31.3

(iii) Regular wave/wind excitation

The hydrodynamic response of the FOWT was analyzed through cases 3 under the condition of single regular wave, where the results are shown in Fig. 14. Because the rotor was still in non-operating state at this time, only the spar platform and tower were modeled. In Fig. 14(a), the heave and pitch RAOs calculated by the present CFD method show good consistency with 3Dfloat and HAWC2 codes. Since the differences in solving methods and ML models between different codes, there are great differences in surge motion RAOs. The dynamic response of the ML is mainly affected by the surge motion. Therefore, combined with the surge motion RAO, the dynamic response amplitude of ML1 is relatively small, as shown in Fig.14(b). Altogether, the results calculated in this study fluctuate within a reasonable range.

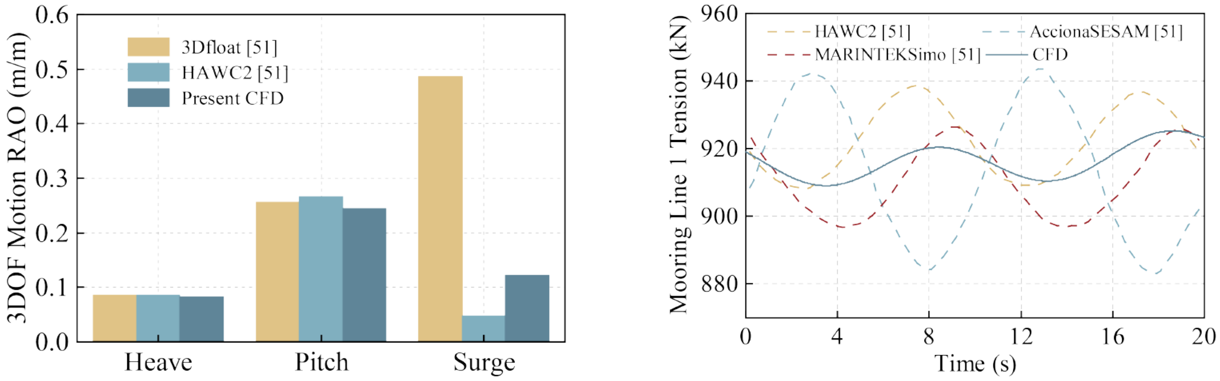

(a) RAO (b) ML responses

Fig. 14. Motion RAO and ML responses of the FOWT.

The aerodynamic response of FOWT under wind only excitation condition is presented in Fig. 15 through calculating the cases 4. From Fig. 15, it is shown that when the blade passes through the tower, the thrust and power responses will fluctuate to a certain extent due to the tower shadow effect. There are three such response fluctuations in one rotation period. In addition to the influence of tower shadow effect, the response curves will also produce a superimposed sinusoidal motion dominated by the natural period of heave. In three heave natural periods, the average amplitudes of thrust and power responses are 18.75 kN and 190.16 kW, respectively. The average thrust and power of the FOWT are 448.03 kN and 1550.01 kW.

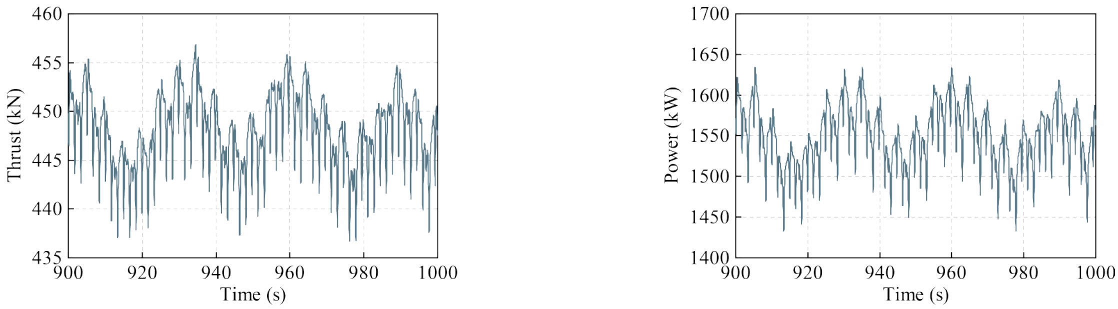

(a) Thrust (b) Power

Fig. 15. Aerodynamic responses of the FOWT under wind only excitation condition.

The hydrodynamic response is further analyzed in Fig. 16. As shown in Fig. 16, different from the case without wave excitation, the heave, pitch and surge response periods of FOWT are all natural periods of the system. In the stage of 1800~2000 s, the average heave response amplitude of the FOWT is 2.894 m, which is significantly higher than 0.426 m when only wave excitation is applied. Unlike the heave response, the pitch response of FOWT does not tend to be stable, with equilibrium position in the total calculation period is of about -0.0482 deg. Consistent with the above free decay results, the surge response period of FOWT is the longest, about 122 s. In 1200~2000 s, the average surge response amplitude of FOWT is 1.761 m, while the response amplitude is 0.611 m under wave only excitation condition. Thus, it is seen that the aero-hydrodynamic response period of FOWT is affected by different excitation conditions, and the response results will be greatly different under this influence.

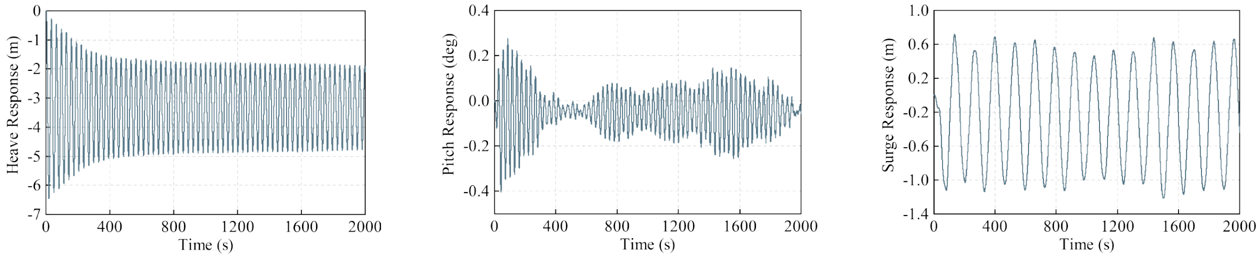

(a) Heave (b) Pitch (c) Surge

Fig. 16. Hydrodynamic responses of the FOWT under wind only excitation condition.

5.2 Influence of heave plate parameters on the hydrodynamic performance

In order to determine the optimal heave plate position, the hydrodynamic responses of top heave plate FOWT (THP-FOWT), middle heave plate FOWT (MHP-FOWT), and bottom heave plate FOWT (BHP-FOWT) are carried out through cases 5, as shown in Fig. 17. Since the aerodynamic responses are not calculated, only the tower and platform are modeled.

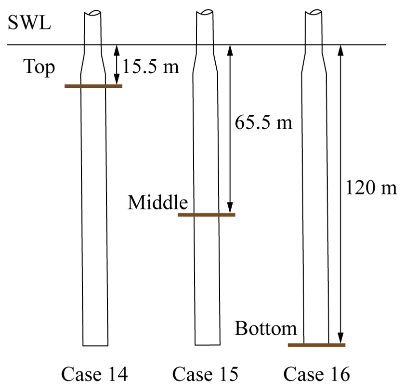

Fig. 17. The heave plate position on the influence of the FOWT.

Before calculating the hydrodynamic performance of the whole system, the free decay tests were carried out on the spar platform with heave plates at different positions, as shown in Fig. 18. Obviously, no matter where the heave plate is installed, it can significantly improve the logarithmic decrement of the heave response of the FOWT system. However, this phenomenon has not been significantly improved in pitch and surge response. The natural properties of the system are further analyzed in Fig. 19. From Fig. 19(a), as the installation position of the heave plate moves down, the natural periods of heave, pitch and surge responses of the FOWTs gradually increases. Overall, due to the structural changes, the natural period changes produced by HP-FOWTs are within a reasonable range. Fig. 19(b) shows the damping ratios of the HP-FOWTs in heave, pitch, and surge responses. In heave response, the damping ratios of BHP-FOWT, MHP-FOWT and THP-FOWT are 11.11%, 9.71% and 12.13%, respectively, which are 359.83%, 301.69% and 402.02% higher than that of the original FOWT (2.41%). In Pitch response, with the heave plate moves down, the pitch damping ratio of HP-FOWTs increases gradually. The maximum pitch damping ratio obtained by BHP-FOWT is 4.24%, which is 20.11% higher than that of the original FOWT (3.53%). For surge damping ratio, the installation of heave plate has no obvious effect. It is seen that the heave plate has a better effect on the improvement of heave modal damping than pitch / surge modal damping.

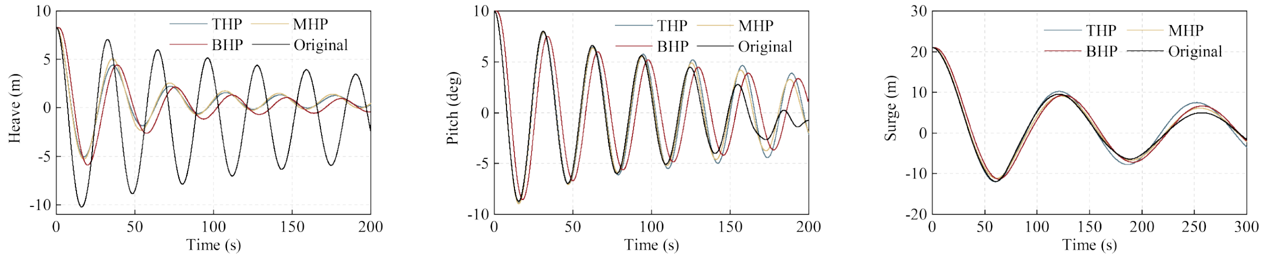

(a) Heave (b) Pitch (c) Surge

Fig. 18. Free decay test under different heave plate positions.

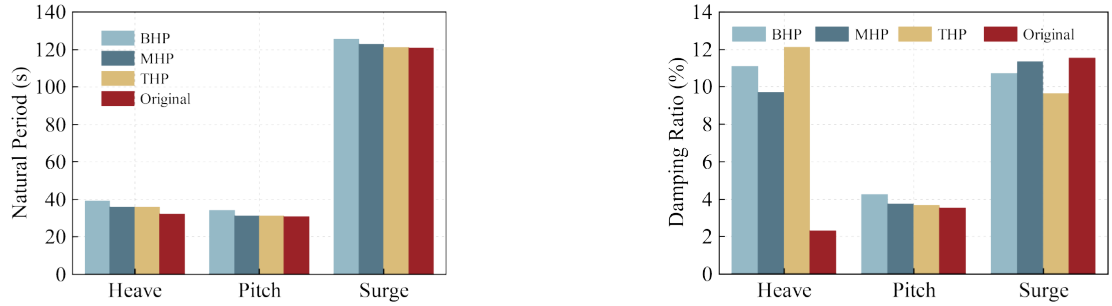

(a) Natural period (b) Damping ratio

Fig. 19. System natural properties of FOWT with different heave plate positions.

Fig. 20 shows the 3DOF responses of the HP-FOWTs, where the original response is performed in case 6 previously. In Fig. 20(a), it is apparent that the stable time of the HP-FOWTs is much shorter than that of the original FOWT because of the increased water displacement and the damping. As the heave plate moves downward the spar platform, the stability time of the heave response increases gradually. The average heave amplitudes of the THP-FOWT, MHP-FOWT, and BHP-FOWT in the stable stage are 0.843 m, 0.451 m, and 0.364 m. Compared with original FOWT (0.414 m), the average amplitudes of the THP-FOWT and MHP-FOWT instead increase by 103.62% and 8.94%, while the BHP-FOWT decreases by 12.08%. And with the heave plate position decreasing, this resonance phenomenon gradually disappears. From Fig. 20(b), the pitch response stabilization time of the original and heave plate FOWTs is basically consistent. The average pitch amplitudes of the THP-FOWT, MHP-FOWT, and BHP-FOWT are 1.223 deg, 1.305 deg and 1.282 deg respectively. Compared with the average amplitude of the original FOWT (1.246 deg), the THP-FOWT decreases by 1.85%, and the MHP-FOWT and BHP-FOWT increase by 4.74% and 2.89%. However, the response standard deviations of the THP-FOWT, MHP-FOWT, and BHP-FOWT are 0.437, 0.488 and 0.470, respectively, decreasing by 14.65%, 4.69% and 8.20%. As the surge responses shown in Fig. 20(c), the standard deviations of the THP-FOWT, MHP-FOWT, and BHP-FOWT are 1.523, 1.246 and 1.356, where the bottom HP-FOWT increases by 2.72% compared with the original one (1.320). In summary, although the pitch and surge response of the BHP-FOWT is slightly worse than that of the original FOWT, it has great advantages in improving the heave response. Therefore, this paper conducts the following research based on the BHP-FOWT.

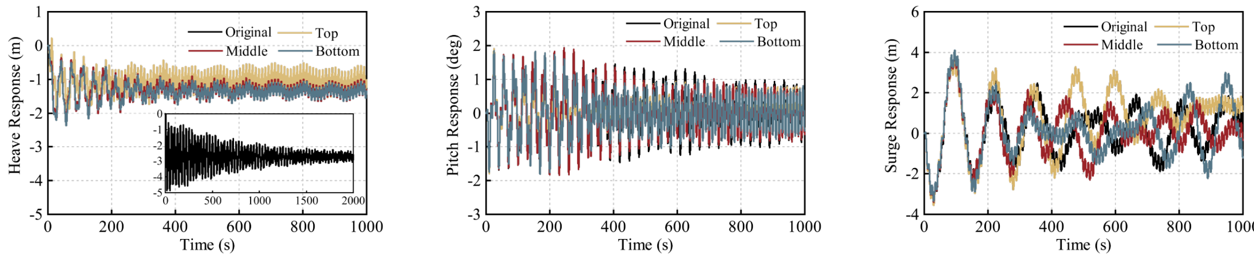

(a) Top (b) Pitch (c) Surge

Fig. 20. Hydrodynamic responses of the FOWT with different installation positions of the heave plate.

5.3 Free decay test of BFHP-FOWTs

Through the above analysis, the heave plate is installed at the bottom of the spar platform, and the bionic fractal structure is applied to the bottom of the Original Heave Plate (OHP) to study the hydrodynamic response. The free decay test results of BFHP-FOWTs obtained by cases 7 are shown in Fig. 21, where the initial displacement in Fig. 21(a) is the position of each research object beyond 10.8 m above its SWL. Obviously, it is observed that the logarithmic decrements of the BFHP-FOWTs and OHP-FOWT are significantly increased compared with the original FOWT. Similar to the above, the BFHP-FOWTs and OHP-FOWT are not much different from the original FOWT in pitch and surge response. By analyzing the properties of BFHP-FOWT system in Fig. 22, it is seen that both BFHPs and OHP increase the natural decay period in heave, pitch and surge directions, where the natural decay periods in heave direction of BFHP-FOWTs and OHP-FOWT are basically the same. It can also be seen from Fig. 22(b) that although the heave damping ratios of BFHP-FOWTs and OHP-FOWT increase gradually, the difference is extremely small, which are 9.841%, 9.872%, 9.913% and 9.857%, respectively, increasing by 585.78%, 587.94%, 590.80% and 586.90% compared with original FOWT (1.435%). As for pitch and surge damping ratios, the BFHP-FOWTs and OHP-FOWT are not found to have a significant improvement effect.

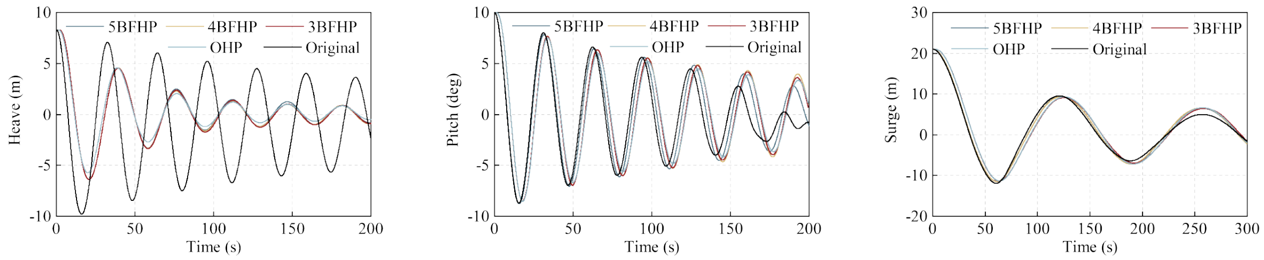

(a) Heave (b) Pitch (c) Surge

Fig. 21. Free decay responses of BFHP-FOWTs.

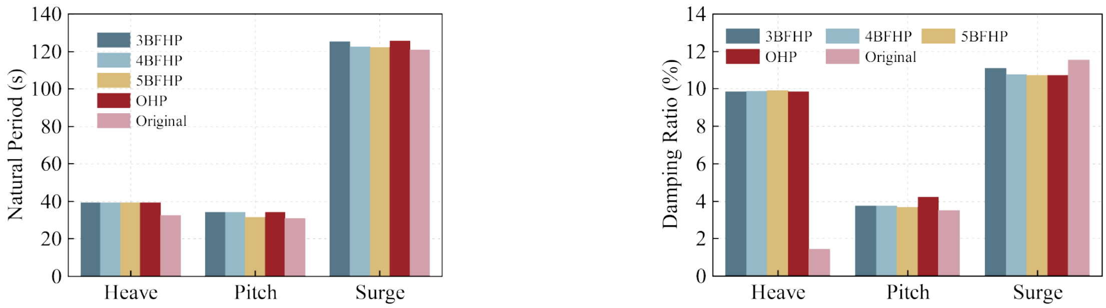

(a) Natural Period (b) Damping ratio

Fig. 22. System Natural properties of BFHP-FOWTs.

Through the above free decay curve analysis, it can be concluded that the BFHP-FOWTs and OHP-FOWT proposed in this study can greatly improve the heave damping ratio, and compared with the original FOWT, the free decay experimental results are within a reasonable range. In harsh sea conditions, the interaction between structures will make the FOWT motion more complex and difficult to predict. Therefore, based on this reliable model, the fully coupled analysis of BFHP-FOWTs under wind and wave excitation conditions is carried out in the next section.

6 Response of the fully-coupled FOWT with BFHP

The response of the fully-coupled FOWT with BFHP (BFHP-FOWT) is investigated in this section, whereas subsection 6.1 deals with the fully-coupled results of the original FOWT. The aerodynamic results of the BFHP-FOWT are analyzed in subsection 6.2, and subsection 6.3 shows the hydrodynamic responses. Table 6 summarizes the cases analyzed in this section.

Table 6

Summary of the cases calculated in this section.

Case	Enabled	Wind Loads	Wave Loads	Analysis Type
8	Platform, tower, rotor	Steady, uniform, V_{hub}=8 m/s	Regular Wave, H_w=6 m, T_w=10 s	Responses of the original FOWT
9	Platform, tower, rotor	Steady, uniform, V_{hub}=11.4 m/s	Regular Wave, H_w=6 m, T_w=10 s	Responses of the original FOWT
10	Platform, tower, rotor, original heave plate	Steady, uniform, V_{hub}=11.4 m/s	Regular Wave, H_w=6 m, T_w=10 s	Responses of the OHP-FOWTs
11	Platform, tower, rotor, 3-Layer BFHP (3BFHP)	Steady, uniform, V_{hub}=11.4 m/s	Regular Wave, H_w=6 m, T_w=10 s	Responses of the 3BFHP-FOWT
12	Platform, tower, rotor, 4-Layer BFHP (4BFHP)	Steady, uniform, V_{hub}=11.4 m/s	Regular Wave, H_w=6 m, T_w=10 s	Responses of the 4BFHP-FOWT
13	Platform, tower, rotor, 5-Layer BFHP (5BFHP)	Steady, uniform, V_{hub}=11.4 m/s	Regular Wave, H_w=6 m, T_w=10 s	Responses of the 5BFHP-FOWT

6.1 Fully-coupled calculation of original FOWT

Given that the above verification results of each coupling part are within a reasonable range, the calculation of the fully-coupled FOWT is carried out in this subsection (case 8). The fully-coupled simulation was calculated for 2000 s until the heave response tended to be stable. The aerodynamic power result of the FOWT is presented in Fig. 23. It is observed in Fig. 23(a) that the power response curve shows periodic reciprocating changes due to the wave excitation, and the period is approximately 10 s. Under both wind and wave loads, the aerodynamic response fluctuation of the FOWT is controlled by the wave period, unlike under wind load only, in which case the fluctuation period is determined by the natural period of the system. Because of the 6DOF motion of the spar platform and the mutual interference of the wake, the power response curve fluctuates greatly in the range of 600~3000 kW compared with the wind only excitation condition. Fig. 23(b) compares the power detail calculated in case 13 with other code results within the two cycles after stabilization. It is seen from Fig. 23(b) that although the power fluctuation amplitude calculated by the present CFD method is significantly higher than that obtained with other codes, it is stable at about 1800 kW, as is the case of other codes. The average power calculated by the present CFD method, FAST, HAWC2, and 3Dfloat codes is 1737 kW, 1719 kW, 1809 kW, and 1871 kW, respectively, which validates the power response calculated by the present CFD method. The reason for the violent fluctuation is that the present CFD method considers flow field effects such as unsteady viscous flow separation, vortex shedding, and free wake; besides, the multiple interference effects between the rotor, nacelle, tower, hub, and platform cannot be neglected; therefore, it is more accurate than traditional numerical analysis codes.

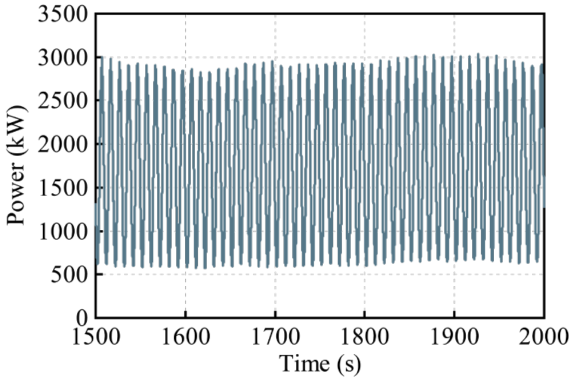

(a) Power

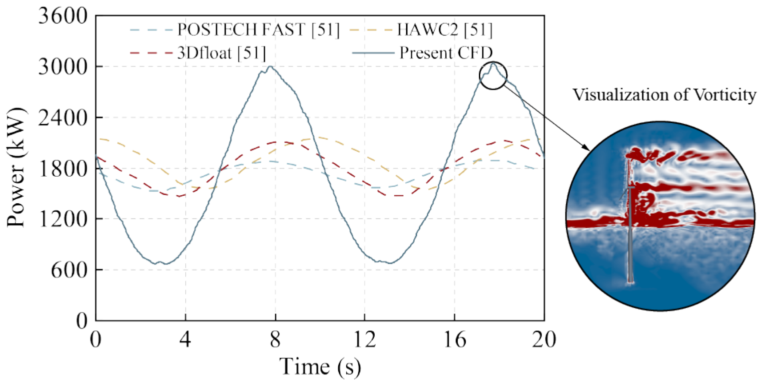

(b) Power details

Fig. 23. Aerodynamic response of the fully-coupled FOWT.

Fig. 24 presents the hydrodynamic responses (6DOF motions) of the fully-coupled FOWT under wind and wave loads. Fig. 24(a) demonstrates the heave response of the FOWT. Because the self-equilibrium position is far away from the SWL, the response period of the FOWT is dominated by the natural period in the range of 0~1000s, and the heave response curve fluctuates with a period of about 31 s. In the range of 1000~2000s, due to the approach to the equilibrium position, the FOWT response period is dominated by the wave period, and the heave curve fluctuates in a period of about 10 s. In the range of 1600~2000 s, the heave response of the FOWT tends to be stable gradually, and the average response amplitude in the 5 cycles after stabilization is approximately 0.411 m. Compared with the heave response, the pitch response (Fig. 24(b)) has a faster stable trend of approximately 800 s. Under wind-wave excitation, the average deviation of the equilibrium position in the pitch response curve is 0.169 deg, while the average response amplitude is about 1.275 deg. In Fig. 24(c), the surge response is also susceptible to wind-wave excitation, leading to an average deviation of 1.201 m in the range of 1000~2000 s. Compared with the average response amplitudes of heave, pitch, and surge (0.426 m, 1.441 deg, 0.611 m) under regular waves only in the same time period, the heave, pitch, and surge response amplitudes of the fully-coupled FOWT are 0.411 m, 1.275 deg, and 0.753 m, respectively – the reason being that the peaks and troughs of the waves under regular wave excitation are more stable and the wavelengths more consistent, which makes the FOWT vulnerable to waves, so the heave and pitch amplitudes are larger than in case 13. In addition, unlike the previous results obtained only under wind load only, the heave and surge response cycles of FOWT under wind and wave loads are mainly affected by the wave period. The response amplitudes of heave and surge responses are obviously lower than that under wind load only, while the amplitude in pitch response increases significantly. Thus, it is concluded that the influence of wave loads on the FOWT is greater than that of wind loads, which is the main factor leading to the change of forced motion mode of FOWT. In Fig. 24(d)~(f), there is a little effect of the wind and wave loads on the sway, roll, and yaw. The average response deviations of the sway, roll, and yaw are 0.034 m, -0.002 deg, and 0.001 deg, respectively. In general, the motion direction directly affected by the wind and wave loads has a greater response amplitude, such as heave, pitch, and surge, while the translation response has a larger response amplitude than the rotation response.

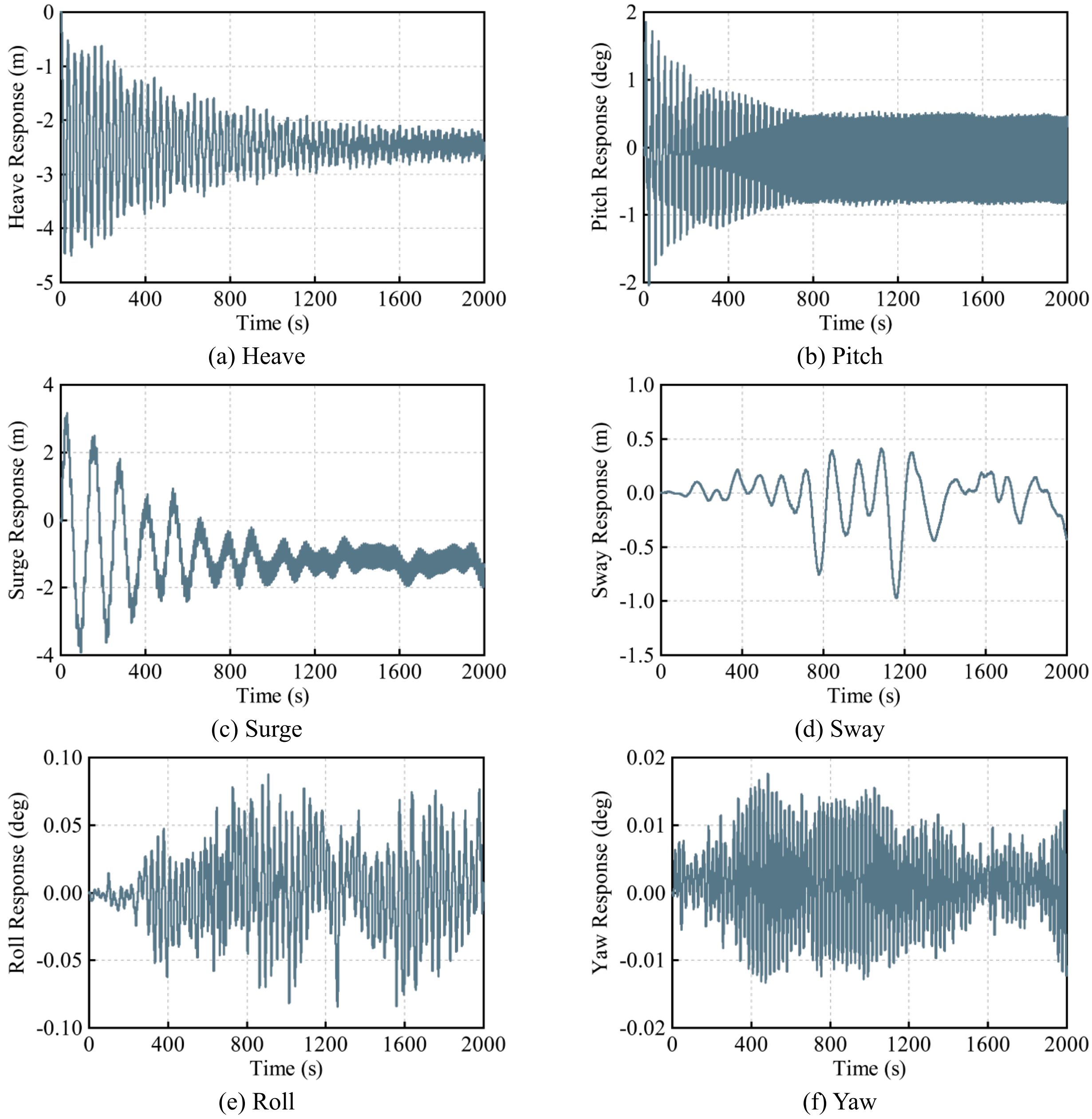

Fig. 24. Hydrodynamic responses of the fully-coupled FOWT.

6.2 Fully-coupled analysis of BFHP-FOWTs

(i) Aerodynamic performance

The aerodynamic response results of the original FOWT, OHP-FOWT, and BFHP-FOWTs are calculated in cases 9~13 (Fig. 25). In Fig. 25(a)~(b), the aerodynamic performances of the BFHP-FOWT are compared to the original FOWT and HP-FOWT. It is seen that the thrust and power of the FOWTs reach a relatively stable fluctuation state after approximately 300 s in the calculated cases. Compared with the 3BFHP-FOWT and 4BFHP-FOWT, the 5BFHP-FOWT has the best stability performance. Since the fractal layers of the HP may lead to the natural periodic variation of the system, the response curves of the 4BFHP-FOWT instead fluctuate greatly. In order to compare the response results more clearly, the partial enlarged details of the thrust and power responses are given in Fig. 25(c)~(d). The results show about a 10 s fluctuation period of the response curve, which is consistent with the wave period. The rotor rotates about 2 circles in a wave period, and the aerodynamic response curve produces a total of 6 significant fluctuations. Because the wind condition of the cases is at rated state, the blade is more vulnerably interfered by the tower, nacelle and hub when passing through the tower, leading to the violent fluctuation of the aerodynamic load and the significant tower shadow effect [52].

In Fig. 25(c), the thrust response amplitudes of the 3BFHP-FOWT and 4BFHP-FOWT are 202.86 kN and 210.25 kN, increasing by 3.73% and 7.51% compared with the original one (195.57 kN) and 4.18% and 7.97% compared with the OHP-FOWT (194.73 kN). The thrust response amplitude of the 5BFHP-FOWT (183.05 kN) decreases by 6.40% compared with the original one and 6.00% compared with the OHP-FOWT. As for the average thrust, the 3~5BFHP-FOWTs increase by 0.57%, 0.89%, and 0.44% compared with the original one, while the OHP-FOWT decreases by 2.62% to the original one. In Fig. 25(d), the power response amplitudes of the OHP-FOWT and 3~5BFHP-FOWTs are 2892.84 kW, 3030.51 kW, 3130.62 kW, and 2734.45 kW, respectively, of which the OHP-FOWT and 5BFHP-FOWT decrease by 0.51% and 5.96% compared with the original FOWT (2907.67 kW). The average power responses of the OHP-FOWT and 3~5BFHP-FOWTs are 4554.36 kW, 4632.99 kW, 4328.74 kW, and 4615.32 kW, respectively, where the 3BFHP-FOWT and 5BFHP-FOWT increase by 1.38% and 0.99% to original FOWT (4570.10 kW). Although the average power of 3BFHP-FOWT is the largest, its standard deviation of 1066.20 is much higher than the original FOWT (974.67). In contrast, the 5BFHP-FOWT obtains the minimum standard deviation of 966.70. Table 7 summarizes the aerodynamic response results of each FOWT. It may be seen that the aerodynamic performance of OHP-FOWT is slightly improved compared with the original FOWT. The fractal layers have a great influence on the response results, of which the aerodynamic performance of 5BFHP-FOWT is significantly improved compared with the original FOWT.

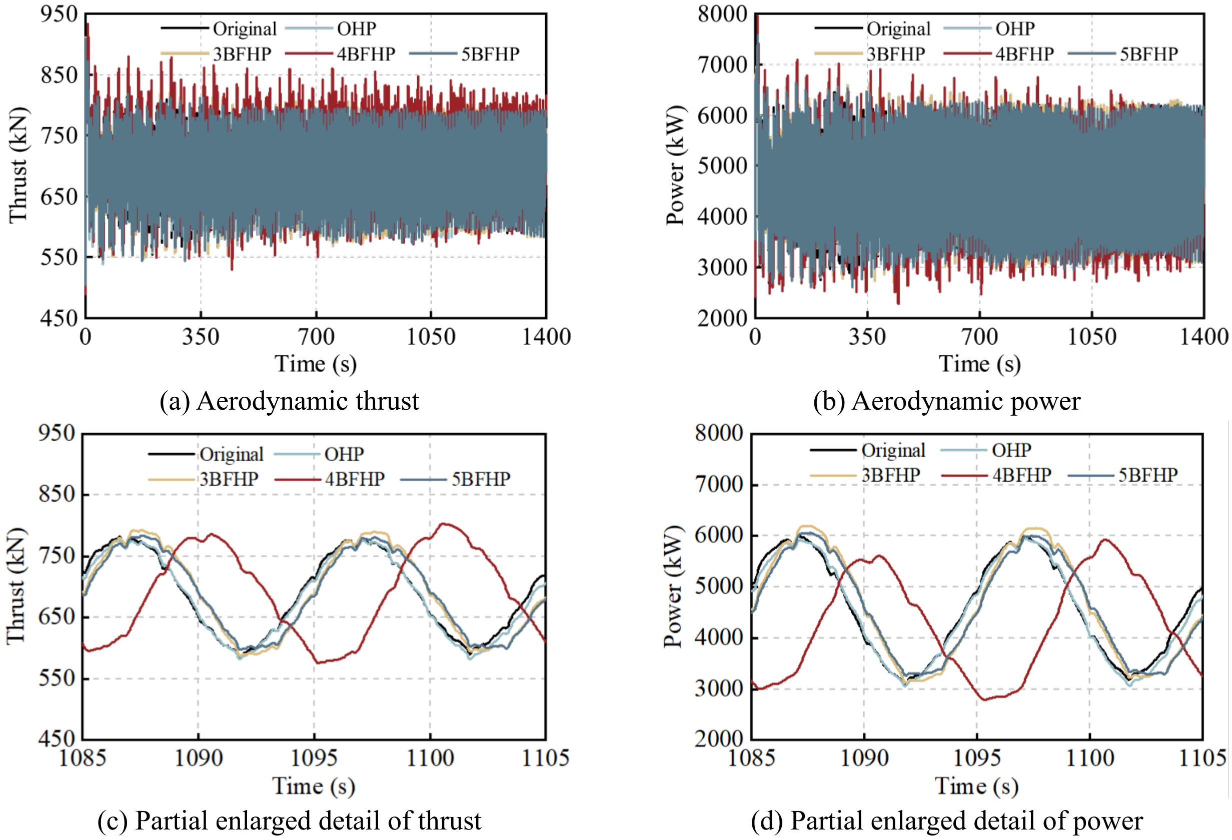

(a) Aerodynamic thrust (b) Aerodynamic power

(c) Partial enlarged detail of thrust (d) Partial enlarged detail of power

Fig. 25. Aerodynamic responses of the BFHP-FOWT.

Table 7

Analysis of the aerodynamic response results.

Aerodynamic Performance	Average Value	Amplitude	Standard Deviation

Thrust (kN)			
Original FOWT	687.75 (-)	195.57 (-)	64.98 (-)
OHP-FOWT	685.94 (-0.26%)	194.73 (-0.43%)	64.95 (-0.05%)
3BFHP-FOWT	691.65 (+0.57%)	202.86 (+3.73%)	70.97 (+9.22%)
4BFHP-FOWT	693.87 (+0.89%)	210.25 (+7.51%)	76.69 (+18.02%)
5BFHP-FOWT	690.75 (+0.44%)	183.05 (-6.40%)	64.25 (-1.12%)
Power (kW)			
Original FOWT	4570.10 (-)	2907.67 (-)	974.67 (-)
OHP-FOWT	4554.36 (-0.34%)	2892.84 (-0.51%)	974.65 (-0.002%)
3BFHP-FOWT	4632.99 (+1.38%)	3030.51 (+4.22%)	1066.20 (+9.39%)
4BFHP-FOWT	4328.74 (-5.23%)	3130.62 (+7.67%)	1051.69 (+7.90%)
5BFHP-FOWT	4615.32 (+0.99%)	2734.45 (-5.96%)	966.70 (-0.82%)

Fig. 26 shows the rotor torque responses of the cases 9~13. Obviously, it is observed that the torque response curves (Fig. 26(a)) gradually fluctuate stably after 300 s calculation. To further analyze the torque response of each FOWT more specifically, the partial enlarged details of the torque are presented in Fig. 26(b). In Fig. 26(b), the rotor torque amplitudes of the OHP-FOWT and 3~5BFHP-FOWTs are 2283.03 kN m, 2391.67 kN m, 2345.79 kN m, and 2158.03 kN m, respectively, where only the OHP-FOWT and 5BFHP-FOWT decrease by 0.51% and 5.96% compared with the original FOWT (2294.72 kN m). The average torque of the cases 9~13 is 3606.71 kN m, 3594.30 kN m, 3656.34 kN m, 3416.23 kN m, and 3642.40 kN m, of which the 3BFHP-FOWT obtains the maximum average torque. By comparing the standard deviation, the 5BFHP-FOWT (762.92) has the optimal stability, while the 3~4BFHP-FOWTs (841.44 and 829.99) have the poor stability, and the OHP-FOWT (769.19) is slightly better than that of the original one (769.21). Thus, it is seen that with the increase of the fractal layer, the effect of fractal structure on the stability of the FOWT gradually increases, of which the 5BFHP-FOWT has the best aerodynamic performance improvement effect, while the stability of the 3~4BFHP-FOWTs instead decrease.

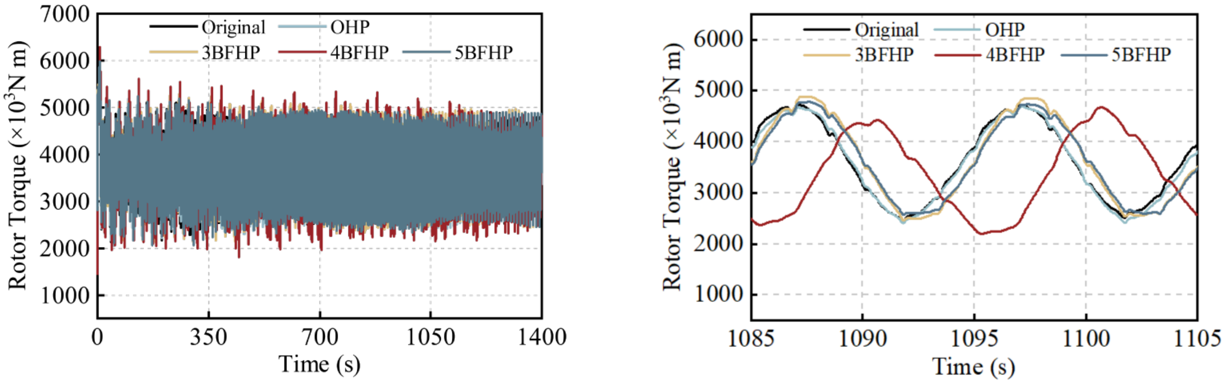

(a) Rotor torque responses (b) Partial enlarged detail of rotor torque

Fig. 26. Rotor torque responses of the BFHP-FOWT.

The analysis of flow field visualization is an advantage of the CFD method, which enables researchers to directly visualize the physical processes of the flow, including the variation conditions of the velocity, pressure, vorticity, etc. Fig. 27 shows the iso-parametric contours of the original FOWT, OHP-FOWT, and BFHP-FOWTs at different times within one wave period. A half of the Y=0 section is used to show the vortices behind the wind turbine through the vorticity method. The vortex tubes are generated by the rotation of the blade tip, which can be identified by Q-Criterion. The fifth-order Stokes wave is generated by the VOF method. Due to the interaction of multiple factors such as the wind-wave loads, 6DOF motion of the platform, blade rotation, and tower and nacelle interference, the aerodynamic performance of the FOWTs varies extremely. The turbulent wake of the FOWTs diffuses backwards from the tower and nacelle in different ways, and eventually dissipates into turbulence. In Fig. 27, it is observed that the wake near the water surface fluctuates more violently since the wind-wave combination. The bound vortices on the vortex tubes continuously falls off the surface of the vortex tubes and interacts with the vortices behind wind turbine, further exacerbating the flow field complexity. In engineering practice, three-dimensional flow visualization helps to better understand the flow characteristics and behaviors of the wakes of the FOWT, thereby optimizing the design of fluid equipment and systems and improving their performance and efficiency. Moreover, the flow field visualization can predict the flow behavior of the FOWT, including the trend of the fluid variation and the stability of the flow, so as to provide a basis for practical engineering applications. It provides a theoretical reference for the application of the BFHP-FOWTs.

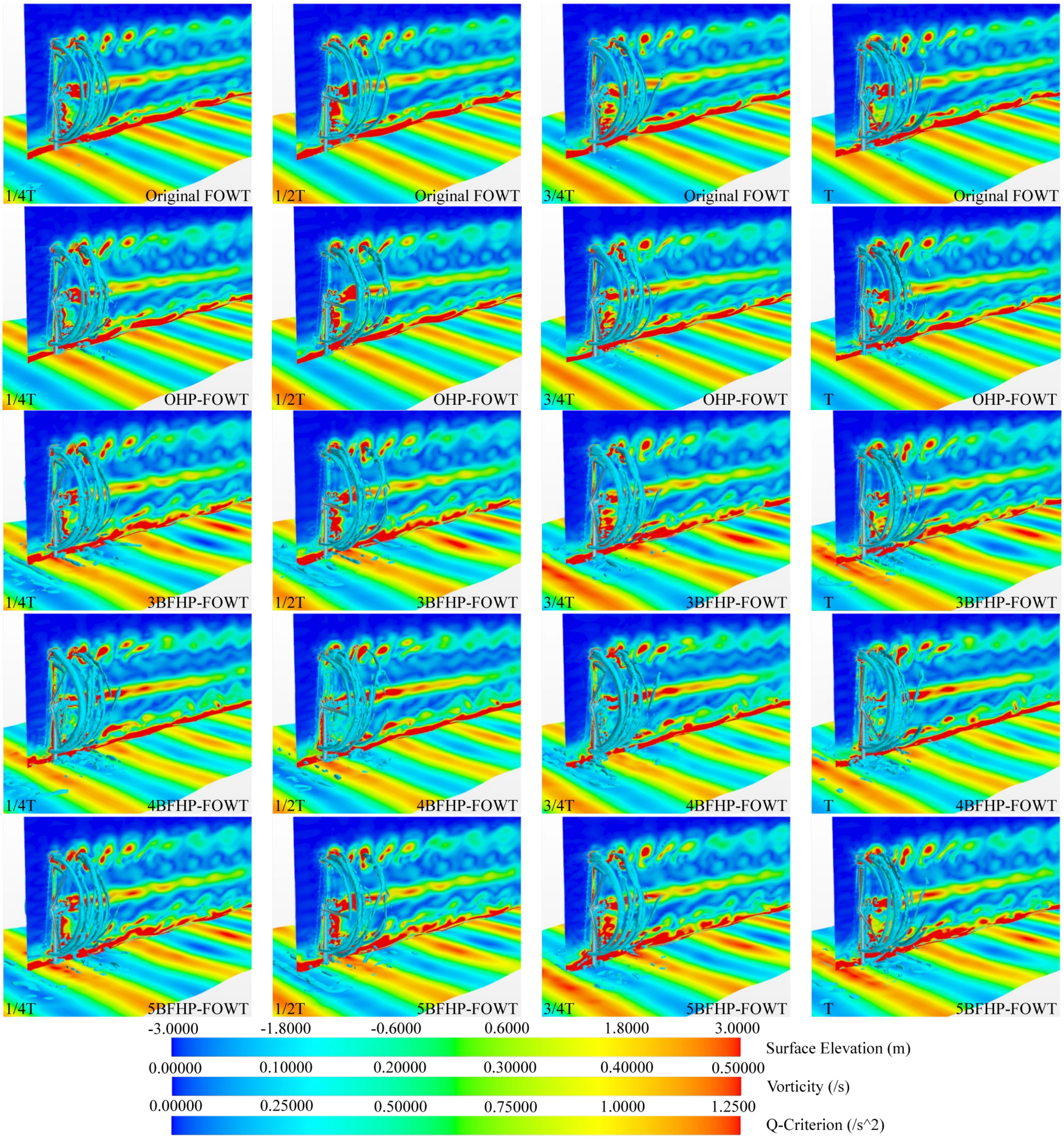

Fig. 27. Instantaneous iso-parametric contours of the FOWTs in three-dimension visualization results.

(ii) Hydrodynamic performance

The hydrodynamic responses of the cases 9~13 are shown in Fig. 28. The total calculation time of the OHP-FOWT and BFHP-FOWTs under the wind-wave excitation conditions is 1400 s, while the total calculation time of the original FOWT is 2000 s. In Fig. 28(a), it is observed that the OHP-FOWT and the BFHP-FOWTs reach a stable response state after about 1050 s, whereas the original FOWT is far from a stable state under the same conditions. Because of the structural and mass changes caused by the installation of the heave plate, the OHP-FOWT and the BFHP-FOWTs have smaller draft depths compared with the original FOWT. In Fig. 28(b), under the influence of the wind-wave combination, the stable position of the pitch response shifts to the direction of wind and wave propulsion. Except for the 4BFHP-FOWT, the pitch response of the other cases reaches a stable state (approximately 600 s) quickly. This is because the variation of the fractal structure has a great influence on the system frequency, which leads to the increase of the amplitude of the 4BFHP-FOWT. The surge responses of the FOWTs are given in Fig. 28(c). The response curves show that the equilibrium position of the surge response is also mainly affected by the wind-wave excitation, of which the deviation of the 5BFHP-FOWT from the original position is the smallest in the later response stage and the 4BFHP-FOWT fluctuates violently due to its certain system attributes. Fig. 28(d)~(f) show the response curves of the remaining 3DOF that are less affected wind-wave excitation. Because the response curves of these 3DOF are irregular, only the standard deviations of the whole calculation time are analyzed. In Fig. 28(d), the sway response standard deviations of the original FOWT, OHP-FOWT, and 3~5BFHP-FOWTs are 0.34, 0.14, 0.25, 0.69, and 0.31, of which the OHP-FOWT has the most stable sway response, while the sway responses of 3BFHP-FOWT and 5BFHP-FOWT are better than that of the original FOWT. In Fig. 28(e), the roll response standard deviations of the 3BFHP-FOWT and 5BFHP-FOWT are 0.067 and 0.086, which are both smaller than the original FOWT (0.091) and OHP-FOWT (0.13). And the 4BFHP-FOWT has the worst stability with a standard deviation of 0.15. As for Fig. 28(f), the yaw response standard deviations of the 3~5BFHP-FOWTs are 0.042, 0.066, and 0.071, respectively. It is shown that the stability of the 3~5BFHP-FOWTs is better than that of the original FOWT (0.074) and OHP-FOWT (0.089), of which the 3BFHP-FOWT obtains the best yaw response stability. Since the distribution positions of the ML2 and ML3 are symmetrical about the Y=0 section, and the sway response has relatively little influence, only the dynamic response of the ML2 is presented, as shown in Fig. 28(g). Because the response of the ML1 is mainly affected by the surge response, its response curve is generally consistent with Fig. 28 (c).

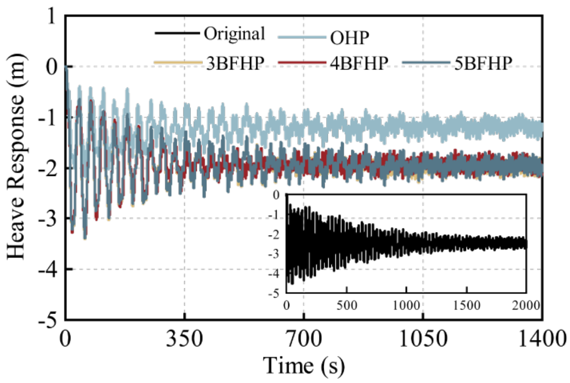

(a) Heave

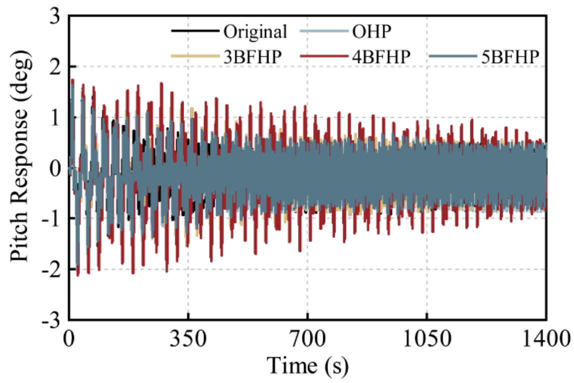

(b) Pitch

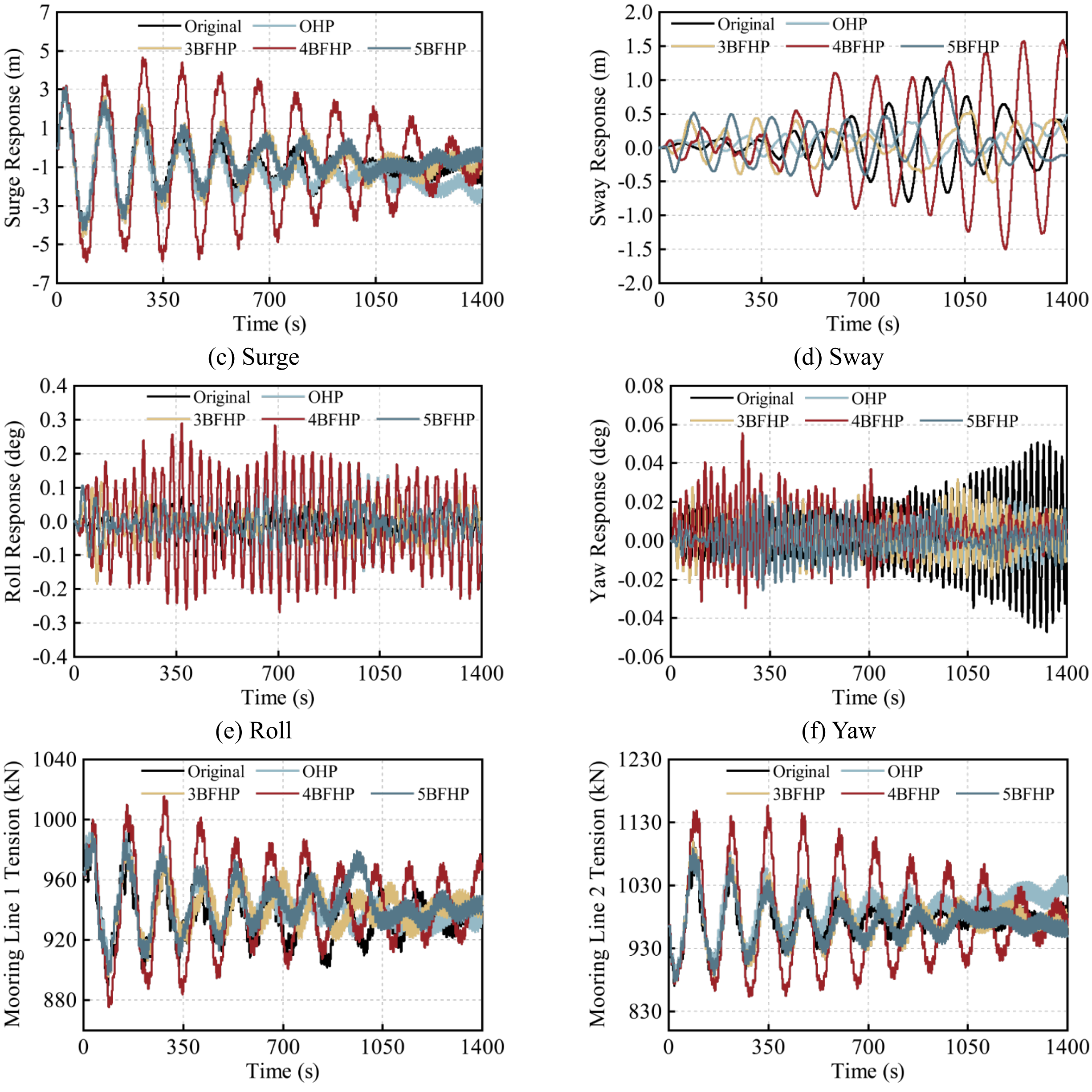

(c) Surge (d) Sway

(e) Roll (f) Yaw

(g) ML1 (h) ML2

Fig. 28. Hydrodynamic responses of the FOWTs.

For the purpose of further analyzing the hydrodynamic performances of cases 9~13, the partial enlarged details within 60 s after stable fluctuation is presented in Fig. 29. The wave period is 10 s, and approximately 6 cycles are analyzed within 60 s. To present more clearly and intuitively, the response amplitudes and standard deviations are summarized in Table 8. As shown in Fig. 29(a), the average heave response amplitudes of the OHP-FOWT and 3~5BFHP-FOWTs are 0.357 m, 0.352 m, 0.340 m, and 0.328 m, decreasing by 18.58%, 19.60%, 22.46%, and 25.03% compared with the original one (0.438 m), respectively. The heave response standard deviations of the 3~5BFHP-FOWTs are 0.132, 0.136, and 0.129, respectively, which are lower than the original FOWT (0.157) and OHP-FOWT (0.143). The standard deviation of the 5BFHP-FOWT shows a maximum decrease of 17.97% compared with the original one, indicating that the 5BFHP-FOWT has the optimal stability in heave response. In Fig. 29(b), the average pitch response amplitudes of the OHP-FOWT and 3~5BFHP-FOWTs are 1.139 deg, 1.289 deg, 1.140 deg, and 1.203 deg, respectively, which are higher than the original FOWT (1.138 deg). Through comparing the pitch response standard deviations, it is seen that the stability of the 3~5BFHP-FOWTs (0.452, 0.530, and 0.424) is worse than that of the original FOWT (0.413) except for the OHP-FOWT (0.403), of which the 4BFHP-FOWT has the worst stability in pitch response. Fig. 29(c) shows the partial enlarged details of the surge responses. Despite the fact that the average surge response amplitudes of the OHP-FOWT (0.638 m) and the 4BFHP-FOWT (0.676 m) decrease by 8.80% and 3.22% compared with the original FOWT (0.699 m), the standard deviations of the OHP-FOWT and 4BFHP-FOWT increase by 9.37% and 13.74%. On the contrary, although the average amplitude of the 5BFHP-FOWT (0.761 m) increases by 8.81% compared to the original FOWT (0.699 m), the 5BFHP-FOWT obtains the optimal stability with a decrease in the standard deviation of 11.44% compared to the original one. Fig. 29(d)~(e) present the partial enlarged details of the ML1 and ML2 responses. The average tension amplitudes of the ML1 obtained by original FOWT, OHP-FOWT, and 3~5BFHP-FOWTs are 11.07 kN, 10.88 kN, 12.08 kN, 6.12 kN, and 12.21 kN, while the ML2 average tension response amplitudes are 24.89 kN, 27.09 kN, 27.18 kN, 24.45 kN, and 26.24 kN, respectively. It is observed that the average amplitudes of the 5BFHP-FOWT have the increases to the original FOWT, however, the 5BFHP-FOWT obtains the best stability with a 17.50% decrease in ML1 standard deviation and 8.25% decrease in ML2 standard deviation. In summary, the BFHP-FOWTs have the excellent performance in improving the heave response of the FOWT. However, in the pitch response, neither the OHP-FOWT nor BFHP-FOWTs have a significant improvement effect. Although the average amplitude of the surge response and ML response is larger than that of the original FOWT, the 5BFHP-FOWT still achieves the best stability performance. Due to the influence of the structural characteristics, the stability of the 4BFHP-FOWT is not ideal in all aspects. Overall, the BFHP-FOWT has a great improvement effect on the stability of the FOWT under a specific number of fractal layers, proving the advantages of the bionic fractal structure in improving the hydrodynamic performance of the FOWT.

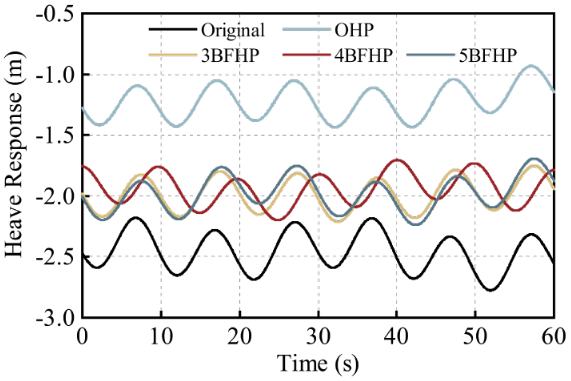

(a) Heave

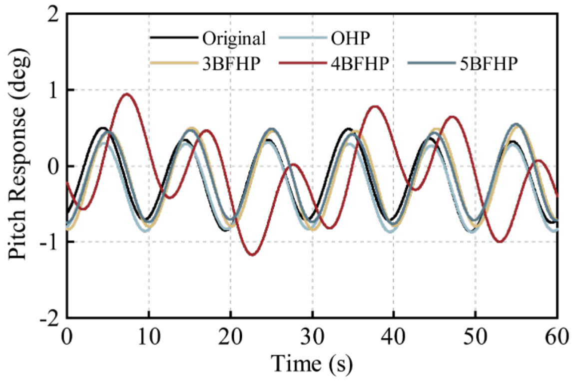

(b) Pitch

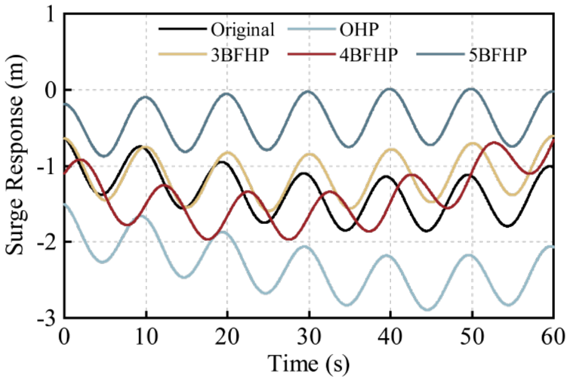

(c) Surge

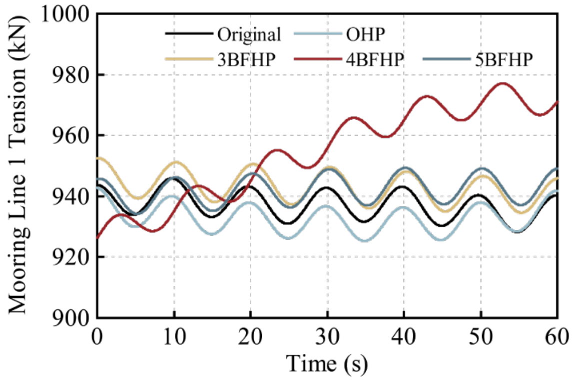

(d) ML1

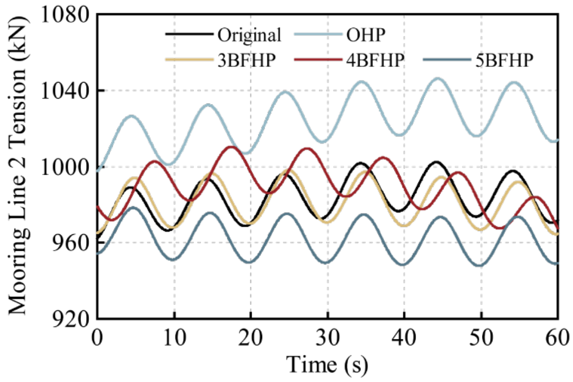

(e) ML2

Fig. 29. Partial enlarged details of the hydrodynamic responses of the FOWTs.

Table 8

Analysis of the hydrodynamic response results.

Hydrodynamic performance	Heave (m)	Pitch (deg)	Surge (m)	ML1 (kN)	ML2 (kN)
Amplitude					
Original FOWT	0.438 (-)	1.138 (-)	0.699 (-)	11.07 (-)	24.89 (-)
OHP-FOWT	0.357 (-18.58%)	1.139 (+0.05%)	0.638 (-8.80%)	10.88 (-1.68%)	27.09 (+8.85%)
3BFHP-FOWT	0.352 (-19.60%)	1.289 (+13.23%)	0.745 (+6.65%)	12.08 (+9.10%)	27.18 (+9.18%)
4BFHP-FOWT	0.340 (-22.46%)	1.140 (+0.16%)	0.676 (-3.22%)	6.12 (-44.73%)	24.45 (-1.18%)
5BFHP-FOWT	0.328 (-25.03%)	1.203 (+5.68%)	0.761 (+8.81%)	12.21 (+10.29%)	26.24 (+5.41%)
Standard deviation					
Original FOWT	0.157 (-)	0.413 (-)	0.302 (-)	5.29 (-)	10.03 (-)
OHP-FOWT	0.143 (-8.85%)	0.403 (-2.35%)	0.330 (+9.37%)	4.40 (-16.90%)	12.13 (+20.98%)
3BFHP-FOWT	0.132 (-15.83%)	0.452 (+9.45%)	0.274 (-9.37%)	4.80 (-9.20%)	9.80 (-2.29%)
4BFHP-FOWT	0.136 (-13.38%)	0.530 (+28.24%)	0.343 (+13.74%)	15.00 (+183.59%)	11.34 (+13.08%)
5BFHP-FOWT	0.129 (-17.97%)	0.424 (+2.72%)	0.267 (-11.44%)	4.36 (-17.50%)	9.20 (-8.25%)

To present the energy absorption effect of the bionic fractal structure, the visualization results of the vortex at the Z=0.25 m section are presented by Q-Criterion. As a commonly used vortex identification method, the Q-Criterion has high computational efficiency and great effect. The specific definitions are as follows:

$$Q=\frac{1}{2}(\|\mathbf{\Omega}\|^2-\|\mathbf{S}\|^2) \quad (15)$$

where the **Ω** is the spin tensor**;** **S** is the strain rate tensor. When the Q value is positive, it represents the vortex-dominated fluid; when the Q value is negative, it denotes the strain-dominated fluid.

Fig. 30 shows the vortex distribution of the Z=0.25 m section in one wave period range (T=10 s). It is observed that there is almost no vortex around the original spar platform at different times in a wave period, which is surrounded by the strain-dominated fluids. The vortices are gradually generated around the heave plate at 1/2 T and 3/4 T as the wave advances, while there is no obvious vortex generation at the stage of 1/4 T and T. Because the branch structure at the bottom of the bionic fractal heave plate forms many cavities, when affected by wave propulsion, the cavity wall interacts with the fluid to form many large and small vortices. The continuous interaction between the vortices and the walls can effectively absorb the wave energy, thus improving the whole system stability. When the number of fractal layers is 3, it is seen that the internal vortex of the cavity has the characteristics of large area and small curl. Compared with the 3BFHP-FOWT, the dense branch structure of the 4BFHP-FOWT decomposes the original large vortex into multiple small vortices. Although the number of the vortices increases, the curl of the vortices is higher only in a few small cavities, and there is almost no vortex generated in many cavities. When the number of fractal layers increases to 5, there is a qualitative change of the vortex distribution in the BFHP. The denser branch structure of the 5BFHP-FOWT decomposes the large vortex into many small vortices. The curl in each cavity is high, and is in full contact with the wall surface, which further increases the contact area, so that the BFHP-FOWT under this fractal layer has the best energy absorption effect. Thus, it is seen that only under a specific number of fractal layers, the bionic fractal heave plate has the best energy absorption effect, which is also the reason why 5BFHP-FOWT has better stability.

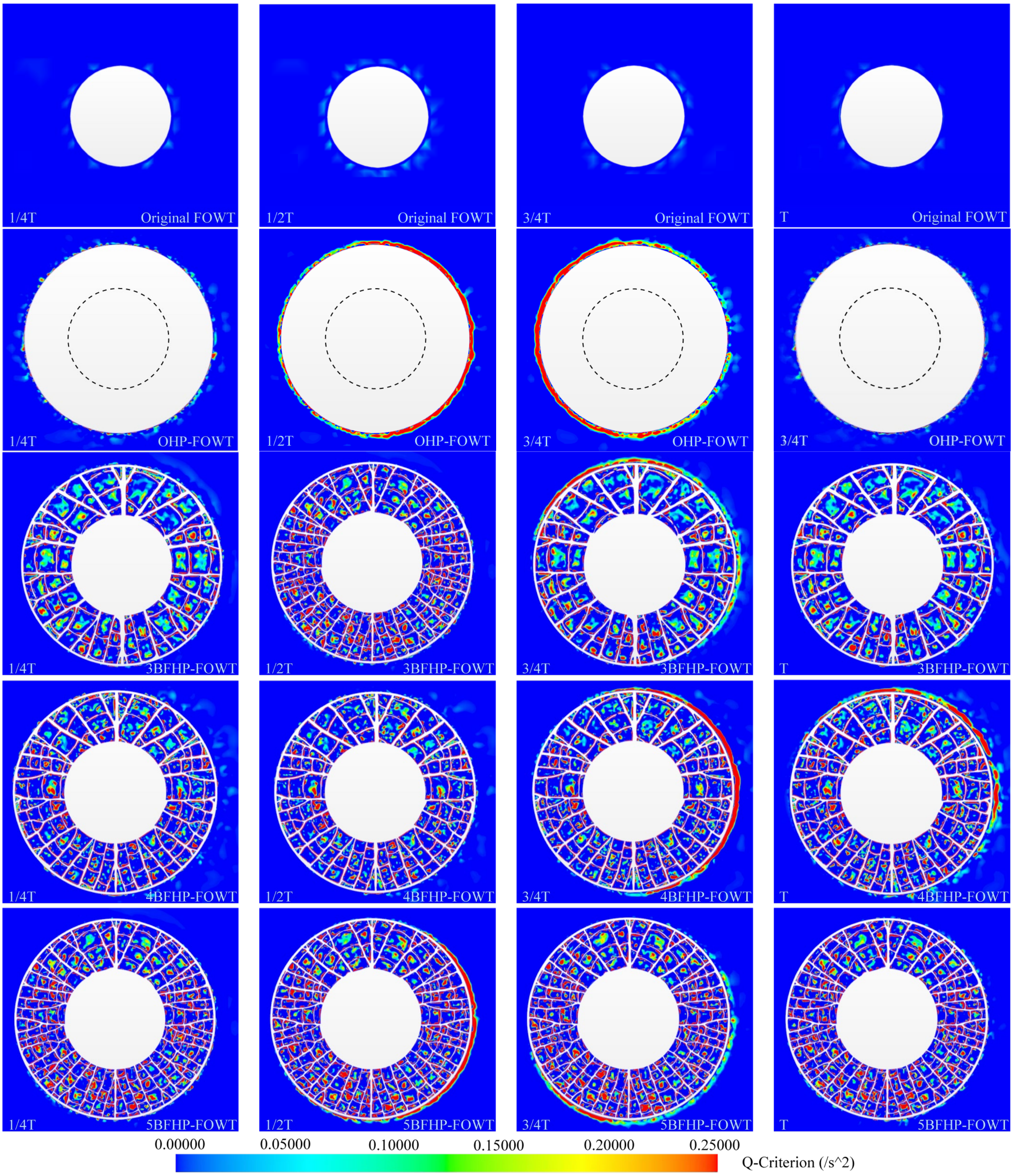

Fig. 30. Visualization results of the FOWTs at Z=0.25 m section.

To further reveal the vortex distribution close to the bionic fractal structure, the visualization results at Z=-0.25 m (below the spar platform) are shown in Fig. 31. It is seen that the vortices are mainly concentrated below the original FOWT, and less around the original spar platform. Unlike the original FOWT, the vortices of the OHP-FOWT are mainly concentrated near the edge of the heave plate, not at the center. This is due to the large diameter of the heave plate, which leads to the weakening of the interaction between the vortices, so that the same central vortices as the original FOWT are not generated. Due to the detachment of the branch structure, the large vortices originally formed in the BFHP structures are decomposed into many small vortices. The open space reduces the vortex curl, but at the same time the number of vortices increases significantly, which aggravates the interaction between vortices and accelerates the dissipation rate of wave energy. As the number of fractal layers increases, the number of vortices does not grow continuously. There is no doubt that the 5BFHP structure produces the largest number of vortices, while the number of vortices under the 4BFHP structure is surprisingly small. This also reflects from the side that the 4BFHP structure has no significant effect on energy absorption, resulting in poor hydrodynamic performance. Through analyzing the vortex distribution around the BFHP structures, it is concluded that 5BFHP-FOWT does have the best performance in energy absorption.

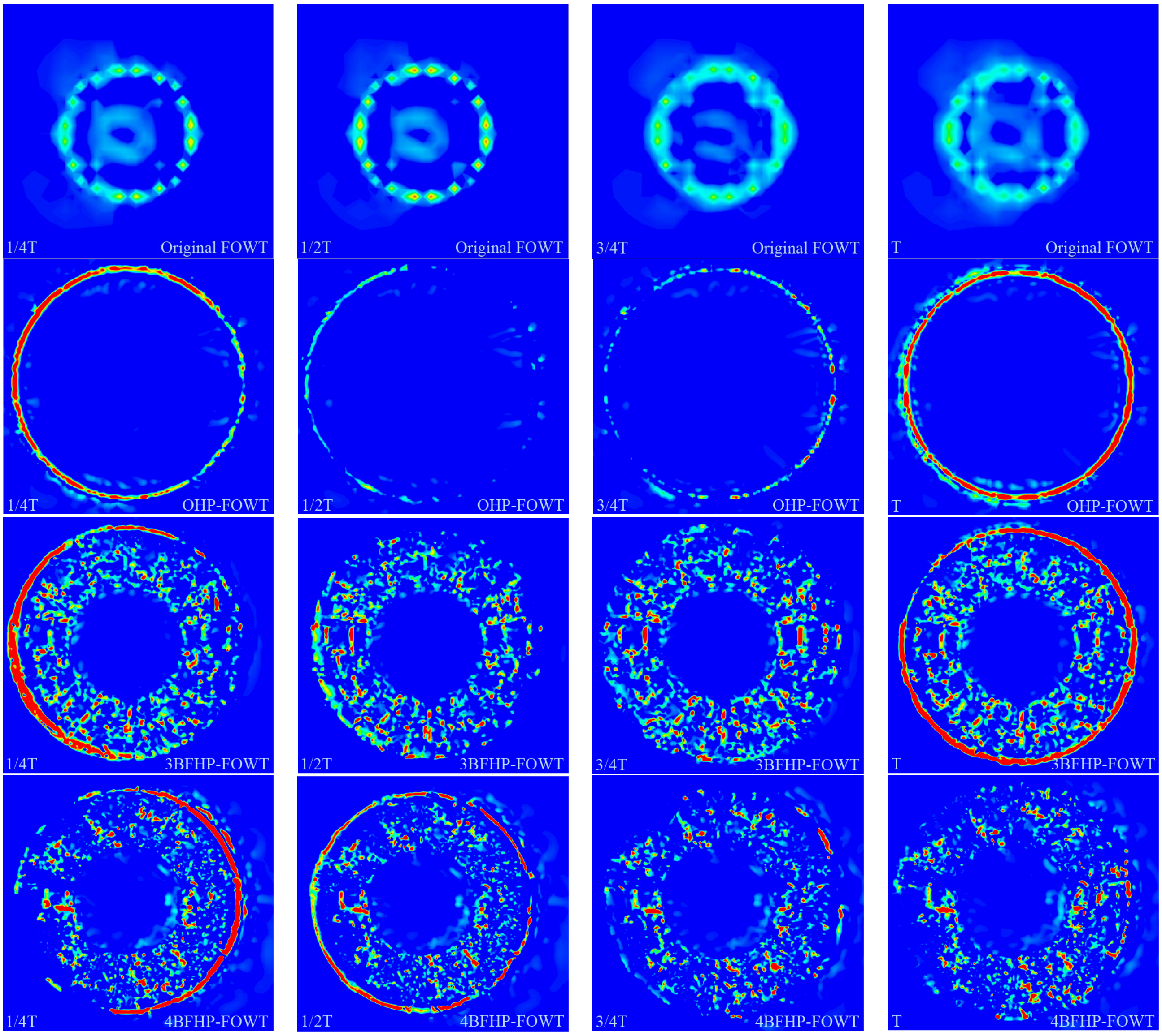

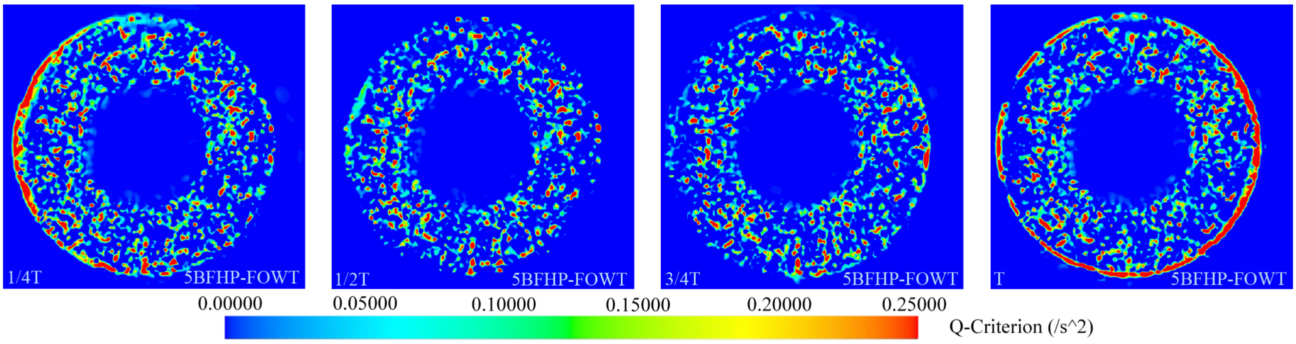

Fig. 31. Visualization results of the FOWTs at Z=-0.25 m section.

7. Conclusion

The NREL 5 MW spar-type FOWT is taken as the research object in this study. The DFBI method combined with the VOF model is used to calculate the fully-coupled responses of the FOWT through the present CFD method. Furthermore, this study proposes a bionic fractal heave plate to improve the stability of the spar-type FOWT. The fractal layers of the bionic fractal heave plate are studied by fully-coupled calculation. The main conclusions are:

(1) The reliability of each coupling part of the FOWT is verified by calculating the aerodynamic power and thrust, free decay tests, RAO responses, and wind only excitation condition. Generally, the response curves show a good agreement with the other simulation codes. The amplitude of heave and surge responses under wave only load is significantly lower than that under wind only load, and the motion period of the FOWT system is controlled by the wave period. By calculating the installation position of the original heave plate, it is found that the bottom heave plate has the best hydrodynamic response. The free decay tests of BFHP-FOWTs show that the hydrodynamic performance of the proposed model can effectively reduce the damping ratio of the system, and the verification results are within a reasonable range.

(2) Through the fully-coupled results under wind-wave excitation conditions, it is shown that the power response amplitude of the FOWT has a larger fluctuation range of 600~3000 kW than other simulation tools. This is because the flow field effect and the complex structure interference are considered in present CFD method. Although the power response fluctuates violently, its average response in one period is 1737 kW, which is within a reasonable range. The hydrodynamic response results of the fully-coupled FOWT present larger average amplitudes compared with the regular wave excitation only in heave and pitch responses. One of the reasons is that the waves excited by a single regular wave are more stable and consistent, making the FOWT vulnerable. Because the direction of the surge response is consistent with the direction of the wind-wave propulsion, the surge response amplitude of the fully-coupled FOWT is larger than that of the FOWT under the single regular wave excitation condition. Overall, the hydrodynamic response of the fully-coupled FOWT is within a relatively reasonable range.

(4) Installing heave plates at different positions of the spar platform has a great influence on the system natural frequency. Of the different options tested numerically, the BHP-FOWT presents the best heave stability. The average heave response of the BHP-FOWT is 0.364 m with a reduction of 12.08%.

(5) From the aerodynamic response results in cases 17~21, the average values of the thrust and power of the OHP-FOWT decrease by 0.26% and 0.34% compared with the original FOWT. The 0.44% increase in average thrust and the 0.99% increase in average power of the 5BFHP-FOWT show that it obtains the best average aerodynamic responses. For the standard deviation, the maximum decreases of 1.12% in thrust response and 0.82% in power response indicate that the 5BFHP-FOWT has the optimal stability; by contrast, the OHP-FOWT presents decreases of 0.05% and 0.002%.

(6) From the three-dimensional visualization results of the calculation domain, it is shown that the wake of the FOWTs interacts with the tower, nacelle, and hub, resulting in violent fluctuations in aerodynamic performance. The vortex tube surfaces generated by the rotation of the blade continuously produces shedding vortices, further

exacerbating the complexity of the flow field.

(7) In hydrodynamic responses of the cases 17~21, the OHP-FOWT and 3~5BFHP-FOWTs present decreases in average heave response amplitudes of 18.58%, 19.60%, 22.46%, and 25.03%, of which the 5BFHP-FOWT obtains a maximum decrease of 17.97% in heave response standard deviation. Compared with the original heave plate, the application of the bionic fractal heave plate will lead to a decrease in the stability of the pitch response. Despite the average surge response amplitude increase of 8.81%, the 5BFHP-FOWT shows the optimal stability with the standard deviation of 11.44% decrease compared with the original FOWT. Although the ML average response amplitudes of the 3BFHP-FOWT and 5BFHP-FOWT increase, their response stability is better than that of OHP-FOWT and 4BFHP-FOWT. Among them, 5BFHP-FOWT obtains the best stability, with decreases in the standard deviations of 17.50% in ML1 and 8.25% in ML2. Under a specific number of fractal layers, the bionic fractal heave plate presents excellent improvement effect on the stability of the FOWT.

(8) The bi-dimensional cut at Z=0.25 m shows that with the increase of fractal layers, the stability improvement of the bionic fractal heave plate does not present a linear trend. Only when the specific fractal layer number is 5, the number and curl of vortices in the cavity increase significantly, showing the best energy absorption effect and stability.

In this study, the FOWTs are regarded as rigid bodies. In the future, fluid-structure interaction research can be carried out on FOWT to better investigate the impact of the complex marine environment. In fact, the internal structure of the Victoria Amazonica is hollow, and the large amount of air filled inside can increase its buoyancy. In view of this, this hollow structure can be applied to the bionic fractal heave plate for subsequent research.

Acknowledgements

The authors would like to acknowledge the support of National Natural Science Foundation of China (Grant No. 51976131, 52006148 and 52106262)

References

[1] Wang P L, Liu Q S, Li C, et al. Effect of trailing edge dual synthesis jets actuator on aerodynamic characteristics of a straight-bladed vertical axis wind turbine. Energy, 2022, 238: 121792.

[2] GWEC. Global Wind Energy Council. Brussels, Global Wind Report, 2022.

[3] Liu Q S., Miao W P., Li C, et al. Effects of trailing-edge movable flap on aerodynamic performance and noise characteristics of VAWT. Energy, 2019, 190: 116271.

[4] Zhou Y, Ning D Z, Chen L F, et al. Experimental investigation on an OWC wave energy converter integrated into a floating offshore wind turbine. Energy Conversion and Management, 2023, 276: 116546.

[5] Chuang T C, Yang W H, Yang R Y. Experimental and numerical study of a barge-type FOWT platform under wind and wave load. Ocean Engineering, 2021, 230: 109015.

[6] Yue M N, Liu Q S, Li C, et al. Effects of heave plate on dynamic response of floating wind turbine Spar platform under the coupling effect of wind and wave. Ocean Engineering, 2020, 201, 107103.

[7] Zhu X Q, Wang, Y F, Yoo W S, et al. Stability analysis of spar platform with four mooring cables in consideration of cable dynamics. Ocean Engineering, 2021,236: 109522.

[8] Li B, Zhou D L, Wang Y. The design of a small lab-scale wind turbine model with high performance similarity to its utility-scale prototype. Renewable Energy, 2020, 149: 435-444.

[9] Sayed M, Klein L, Lutz Th, et al. The impact of the aerodynamic model fidelity on the aeroelastic response of a multi-megawatt wind turbine. Renewable Energy, 2019, 140: 304-318.

[10] Sebastian T, Lackner M A. Development of a free vortex wake method code for offshore floating wind turbines. Renewable Energy, 2012, 46: 269-275.

[11] Dynnikova G Y, Guvernyuk S V, Demchenko Y V, et al. An efficient algorithm for calculating boundary elements in vortex methods. Engineering Analysis with Boundary Elements, 2023, 151: 394-399.

[12] Broek M J, Tavernier D D, Sanderse B, et al. Adjoint optimisation for wind farm flow control with a free-vortex wake model. Renewable Energy, 2022, 201: 752-765.
[13] Wang Y, Chen H C, Koop A, et al. Hydrodynamic response of a FOWT semi-submersible under regular waves using CFD: Verification and validation. Ocean Engineering, 2022, 258: 111742.
[14] Wang L, Robertson A, Kim J, et al. Validation of CFD simulations of the moored DeepCwind offshore wind semisubmersible in irregular waves. Ocean Engineering, 2022, 260: 112028.
[15] Puhan P, Awasthi A, Mukherjee A K, et al. CFD modeling of segregation in binary solid-liquid flfluidized beds: Inflfluence of liquid viscosity and density. Chemical Engineering Science, 2021, 246: 116965.
[16] Rezaeiha A, Micallef, D. Wake interactions of two tandem flfloating offshore wind turbines: CFD analysis using actuator disc model. Renewable Energy, 2021, 179: 859-876.
[17] Fang Y, Li G, Han Z L, et al. Effect of surge motion on rotor aerodynamics and wake characteristics of a floating horizontal-axis wind turbine. Energy, 2021, 218: 119519.
[18] Guo Y, Wang X D, Mei Y H, et al. Effect of coupled platform pitch-surge motions on the aerodynamic characters of a horizontal floating offshore wind turbine. Renewable Energy, 2022, 196: 278-297.
[19] Oliveira M, Puraca R C, Carmo B S. Blade-resolved numerical simulations of the NREL offshore 5 MW baseline wind turbine in full scale: A study of proper solver confifiguration and discretization strategies. Energy, 2022, 254: 124368.
[20] Quallen S, Xing, T. CFD simulation of a floating offshore wind turbine system using a variable-speed generator-torque controller. Renewable Energy, 2016, 97: 230-242.
[21] Liu Y C, Xiao Q, Incecik A, et al. Establishing a fully coupled CFD analysis tool for floating offshore wind turbines. Renewable Energy, 2017, 112: 280-301.
[22] Rao M J, Nallayarasu S, Bhattacharyya S K. CFD approach to heave damping of spar with heave plates with experimental validation. Applied Ocean Research, 2021, 108: 102517.
[23] Hegde P, Nallayarasu S. Hydrodynamic response of buoy form spar with heave plate near the free surface validated with experiments. Ocean Engineering, 2023, 269: 113580.
[24] Rao M J, Nallayarasu S, Bhattacharyya S K. Numerical and experimental studies of heave damping and added mass of spar with heave plates using forced oscillation. Applied Ocean Research, 2021, 111: 102667.
[25] Subbulakshmi A, Jose J, Sundaravadivelu R, et al. Effect of Viscous Damping on Hydrodynamic Response of Spar with Heave Plate. Aquatic Procedia, 2015, 4: 508-515.
[26] Lu Q X, Guan Y, Fu S H. Self-driven super water vapor-absorbing calcium alginate-based bionic leaf for Vis-NIR spectral simulation. Carbohydrate Polymers, 2022, 296: 119932.
[27] Cooper L N, Sedano N, Johansson S, et al. Hydrodynamic performance of the minke whale (Balaenoptera acutorostrata) flipper. The Journal of Experimental Biology, 2008, 211: 1859-1867.
[28] Mohammadi H, Ahmad Z, Petru M, et al. An insight from nature: honeycomb pattern in advanced structural design for impact energy absorption. Journal of Materials Research and Technology, 2023, 22: 2862-2887.
[29] Cui Y C, Chen L, Feng S, et al. Novel cuttlebone-inspired hierarchical bionic structure enabled high energy absorption. Thin-Walled Structures, 2023, 186: 110693.
[30] Fu J, Liu Q, Liufu K M, et al. Design of bionic-bamboo thin-walled structures for energy absorption. Thin-Walled Structures, 2019, 135: 400-413.
[31] Peng Y, Li T, Bao C H, et al. Performance analysis and multi-objective optimization of bionic dendritic furcal energy-absorbing structures for trains. International Journal of Mechanical Sciences, 2023, 246: 108145.
[32] Wang C Y, Li Y, Zhao W Z, et al. Structure design and multi-objective optimization of a novel crash box based on biomimetic structure. International Journal of Mechanical Sciences, 2018, 138-139: 489-501.

[33] Rian I M, Sassone M. Tree-inspired dendriforms and fractal-like branching structures in architecture: A brief historical overview. Frontiers of Architectural Research, 2014, 3: 298-323.

[34] Zhao L, Ma J F, Chen W Y, et al. Lightweight Design and Verification of Gantry Machining Center Crossbeam Based on Structural Bionics. Journal of Bionic Engineering, 2011, 8: 201-206.

[35] He Q, Wang Y H, Shi X N, et al. Crushing behavior on the cylindrical tube based on lotus leaf vein branched structure. Mechanics of Materials, 2022, 165: 104205.

[36] Li P, Sun J L, Cai M F, et al. Acoustic emission behavior of rock materials containing two preexisting flaws and an opening subjected to uniaxial compression: insights into self-similarity, chaotic, and fractal features. Journal of Materials Research and Technology, 2022, 20: 1786-1801.

[37] Mandelbrot B. How long is the coast of Britain? Statistical self-similarity and fractional dimension. Science, 1967, 156(3775): 636-638.

[38] Wang J, Zhang Y, He N, et al. Crashworthiness behavior of Koch fractal structures. Materials and Design, 2018, 144: 229-244.

[39] Li Z D, Shen L M, Wei K, et al. Compressive behaviors of fractal-like honeycombs with different array configurations under low velocity impact loading. Thin-Walled Structures, 2021, 163: 107759.

[40] Bovill C. Fractal Geometry in Architecture and Design. Nexus Network Journal, 1996, 3: 145-146.

[41] Jonkman J. Definition of the Floating System for Phase IV of OC3. America: NREL, 2010.

[42] Jonkman J, Butterfield S, Musial W, et al. Definition of a 5-MW reference wind turbine for offshore system development. America: NREL, 2009.

[43] Miao W P, Liu Q S, Xu Z F, et al. A comprehensive analysis of blade tip for vertical axis wind turbine: Aerodynamics and the tip loss effect. Energy Conversion and Management, 2022, 253: 115140.

[44] Ishihara T, Qian G W. A new Gaussian-based analytical wake model for wind turbines considering ambient turbulence intensities and thrust coefficient effects. Journal of Wind Engineering & Industrial Aerodynamics, 2018, 177: 275-292.

[45] Wang Y, Wang L, Jiang Y, et al. A new method for prediction of power coefficient and wake length of a horizontal axis wind turbine based on energy analysis. Energy Conversion and Management, 2022, 252: 115121.

[46] Choiniere M, Davis J, Nguyen N, et al. Hydrodynamics and load shedding behavior of a variable-geometry oscillating surge wave energy converter (OSWEC). Renewable Energy, 2022, 194: 875-884.

[47] D'Angiò D, Lenti L, Martino S. Microseismic monitoring to assess rock mass damaging through a novel damping ratio-based approach. International Journal of Rock Mechanics and Mining Sciences, 2021, 146: 104883.

[48] Fenton J D. A Fifth-Order Stokes Theory for Steady Waves. Journal Of Waterway Port Coastal And Ocean Engineering, 1985, 111(2): 216-234.

[49] Huang H D, Liu Q S, Yue M N, et al. Fully coupled aero-hydrodynamic analysis of a biomimetic fractal semi-submersible floating offshore wind turbine under wind-wave excitation conditions. Renewable Energy, 2023, 203: 280-300.

[50] Cheng P, Huang Y, Wan D C. A numerical model for fully coupled aero-hydrodynamic analysis of floating offshore wind turbine. Ocean Engineering, 2019, 173: 183-196.

[51] Jonkman J, Musial W. Offshore Code Comparison Collaboration (OC3) for IEA Task 23 Offshore Wind Technology and Deployment. America: NREL, 2010.

[52] Orlando S, Bale A, Johnson D A. Experimental study of the effect of tower shadow on anemometer readings. Journal of Wind Engineering and Industrial Aerodynamics, 2011, 99: 1-6.